

pubs.acs.org/cm Article

Tuning the Solution Aggregate Structure of a PM7-Based Conjugated Polymer to Enable Green Solvent Processing of Organic Solar Cells

Published as part of Chemistry of Materials virtual special issue "In Honor of Prof. Elsa Reichmanis".

Azzaya Khasbaatar, Austin L. Jones, Pravini S. Fernando, Hiroaki Sai, Chenhui Zhu, Eliot Gann, John R. Reynolds, and Ying Diao*



Cite This: Chem. Mater. 2024, 36, 2819-2834



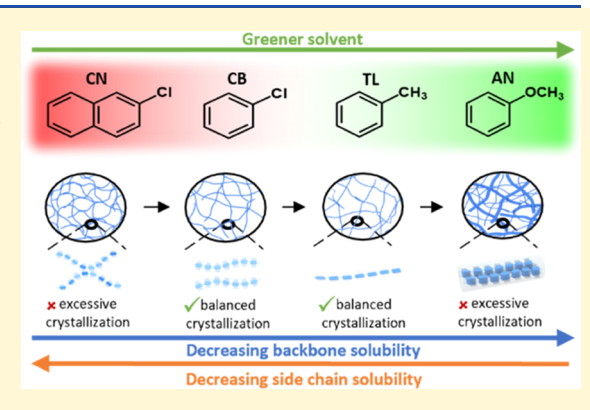
ACCESS

III Metrics & More

Article Recommendations

s) Supporting Information

ABSTRACT: Understanding how solvents influence the solution-state aggregation of conjugated polymers and film morphology is crucial for solution-processed organic solar cells (OSCs). Herein, using the conjugated donor polymer PM7 D2, a more processable derivative of PM7 that readily dissolves in a range of halogenated and nonhalogenated (green) solvents, we find that solvent affinity toward the polymer backbone, as opposed to the alkyl side chains, drastically tunes the polymer solution aggregate structures and the resultant blend film morphologies. Our findings reveal that using a poor side-chain solvent forms semiflexible amorphous networks with strong side-chain associations, whereas using a poor backbone solvent leads to semicrystalline fiber aggregates. On the other hand, mutual solvents, which balance the polymer backbone and side-chain solubility, result in rigid amorphous networks



with weak/no side-chain interactions. Upon film deposition via blade coating, both semicrystalline fibers and flexible amorphous network aggregates of PM7 D2 yield highly crystalline films with large domains. In contrast, rigid amorphous aggregates with weak or no side-chain associations prevented excessive crystallization of PM7 D2. We found that the green solvent studied in this work (anisole) exhibits poor affinity toward the backbone but is selective to the alkyl side chains, thus forming semicrystalline fibers in solution. Consequently, PM7 D2:ITIC-4F-based OSCs cast from the green solvent only exhibit 5.8% efficiency. Interestingly, similar to using mutual solvents, utilizing hot solution processing converts the semicrystalline fibers to rigid amorphous network aggregates by increasing the backbone solubility, thereby suppressing the excessive crystallization of PM7 D2. Ultimately, the devices exhibited a significant power conversion efficiency (PCE) improvement from 5.8 to 9%, where they were fully processed and tested under ambient conditions in a glovebox-free environment (without additives).

INTRODUCTION

Owing to the development of non-fullerene-based molecular acceptors, the efficiency of OSCs has rapidly progressed over the past decade, triggering a renaissance in the field. Remarkably, power conversion efficiencies (PCEs) have now surpassed 19% in single junction cells, 1-5 enabling opportunities for the successful commercialization of organic solar cells (OSCs). Despite these advances, processing of these highly efficient OSCs often involves toxic halogenated solvents, which pose serious health and environmental risks.^{6,7} Therefore, using less toxic nonhalogenated or green solvents is crucial for the ecofriendly processing of OSCs, particularly for large-scale manufacturing. Green solvent-processed OSCs, however, often underperform devices processed from halogenated solvents due to the limited solubility of donor-acceptor-based conjugated polymers in most nonhalogenated solvents, yielding undesirable film morphologies. To overcome this challenge, molecular

engineering approaches have been utilized to increase the solubility of conjugated polymers to improve the processability of OSCs in green solvents. These approaches mainly involve increasing the side-chain length of the conjugated polymer to improve solubility and functionalizing the side chains or the backbone to decrease the backbone rigidity to reduce intermolecular interactions. While molecular design approaches have significantly contributed to improving the solubility of conjugated polymers in green solvents, enhancing

Received: December 2, 2023
Revised: February 14, 2024
Accepted: February 16, 2024
Published: March 5, 2024





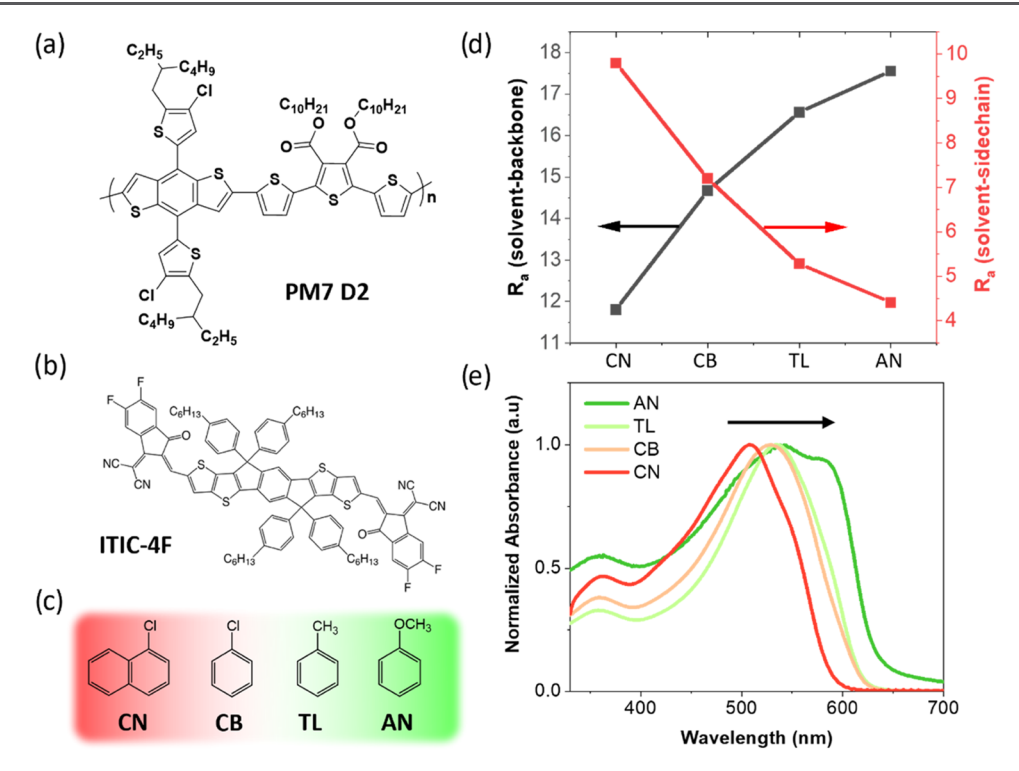


Figure 1. Molecular structures of (a) PM7 D2, (b) ITIC-4F, and (c) solvents (CN – 1-chloronaphthalene, CB – chlorobenzene, toluene – TL, anisole – AN) used in this study. (d) Hansen solubility distance (R₃) comparison for the conjugated backbone and the side chain of PM7 D2, depending on the solvent. (e) UV–vis spectra of PM7 D2 solutions (20 mg/mL) in these four solvents.

the solubility via molecular design alone has not been sufficient to close the performance gap, suggesting that further morphology improvements are needed for green solvent-processed OSCs.

Conjugated polymers typically undergo self-assembly processes in solution via $\pi - \pi$ stacking and side-chain interactions, leading to polymer aggregates that substantially impact the solid-state morphology. Numerous studies have shown that solution-state aggregation of conjugated polymers enhances alignment, 14,15 crystallinity, 16–18 and out-of-plane molecular orientation. Aggregation of conjugated donor polymers in solution has also been found to be advantageous for OSCs as it prevents large-scale phase segregation caused by liquid-liquid demixing in both fullerene and other molecular acceptor (MA)based systems. 21-23 Notably, Wang and Bredas et al. proposed that the extent of aggregation of conjugated polymers, determined by the Flory-Huggins interaction parameter, has a strong correlation with film morphology, particularly domain sizes and crystal coherence lengths.²⁴ Besides the extent of aggregation of conjugated polymers, the structure of polymer aggregates in solution plays an important role in the morphology and device performance of OSCs. Our previous work revealed that amorphous network aggregates are beneficial for the morphology of MA-based OSCs, leading to small domains with predominantly face-on molecular orientation.²²

When transitioning from halogenated to nonhalogenated solvents, a change in the solution-state aggregation behavior is inevitable, as nonhalogenated solvents are often poor solvents for conjugated polymers. Therefore, understanding how the solvent environment influences the aggregation and assembly behavior of conjugated polymers is crucial for enhancing the active layer morphology of green solvent-processed OSCs. Previous studies have shown that the nature and extent of solution-state aggregation of conjugated polymers is highly

dependent on the quality of solvents toward conjugated polymers.²⁶ For instance, using small-angle X-ray scattering (SAXS), Nahid and McNeill et al. have shown that solution-state aggregation of the P(NDI2OD-T2) polymer (repeat unit structure shown in Figure S1a) changes from coil-like polymer chains in good solvents to elongated rigid-like aggregates in poor solvents, which enhanced molecular ordering in thin films and maximized the device performance of organic field effect transistor (OFET) devices.²⁶ Similarly, using SAXS and freeze-dried imaging, Zheng and Pei et al. found that the BDOPV-based conjugated polymer (repeat unit structure shown in Figure S1b) can form either a 1D rod-like structure in a good solvent or 2D lamellar aggregates in a poor solvent, which is then directly inherited to the solid state, improving the charge mobility from 1.8 to 3.2 cm² V⁻¹ s⁻¹ in OFETs. ²⁷ Besides influencing the initial solution aggregate structures, solvents can also tune the assembly pathways of conjugated polymers during solution processing. ^{28,29} Our group has previously reported that tuning the solvent selectivity toward conjugated backbone versus side chains of the PII-2T polymer led to three distinct assembly pathways, which are direct crystallization, liquid crystal (LC)-mediated crystallization, and random agglomeration during solution processing.²⁹ When using a backbone-selective solvent 1-chloronaphthalene, direct crystallization of the conjugated polymer led to the highest degree of film alignment and thus a 20-fold increase in the charge mobility compared to LC-mediated crystallization and random agglomeration pathways. Although solvents can drastically influence solution-state aggregation and assembly pathways of conjugated polymers from the solution to the solid state, their implications on BHJbased OSCs are rarely investigated, particularly for green solvent-processed OSCs. Therefore, the purpose of this study is to examine the polymer aggregate structure—assembly morphology relationship in the context of green solvent processing.

Herein, using a benzodithiophene-based donor polymer (PM7 D2)³⁰ as our model system and a range of halogenated and nonhalogenated solvents, we demonstrate how solvent properties, particularly solvent-backbone and solvent-side chain interactions, impact the polymer solution-state aggregate structures and their crystallization behavior. The donor polymer PM7 D2 is chosen in this study due to its good solubility in a wide range of halogenated and nonhalogenated solvents compared to its counterpart, PM7, which strongly aggregates even in chlorobenzene because of its highly planar backbone.²⁵ Depending on the solvent properties, three distinct aggregate structures of PM7 D2 were obtained: semiflexible amorphous networks in a poor side-chain solvent, rigid amorphous networks in mutual solvents, and semicrystalline fiber aggregates in a poor backbone solvent. Upon film deposition, both semiflexible amorphous network and semicrystalline fiber aggregates led to highly crystalline films with large domains, yielding 7.1 and 5.8% PCEs in PM7 D2:ITIC-4F-based devices, respectively. In contrast, rigid amorphous network aggregates formed in mutual solvents achieved a more balanced crystallization of PM7 D2, resulting in PCEs of 8-9%, with devices being fully fabricated under ambient conditions. Importantly, we demonstrate that the semicrystalline fiber aggregates formed in the poor backbone solvent anisole, the green solvent studied in this work, undergo an order-to-disorder transition to form rigid amorphous network aggregates at high temperatures. Consequently, processing PM7 D2:ITIC-4F-based devices at elevated temperatures when cast from the green solvent substantially enhanced the device performance from 5.8% to 9.0%. Our findings thus highlight that forming rigid amorphous network aggregates, compared to crystalline fiber aggregates or semiflexible amorphous network aggregates, is critical to achieving a favorable blend film morphology, thereby enabling green solvent processing of nonfullerene organic solar cells.

RESULTS AND DISCUSSION

Materials Systems and Solvent Properties. Figure 1a shows the repeat unit structure of the conjugated donor polymer, PM7 D2, used in this study (the synthesis results are tabulated in Table S1). First reported by Jones and Reynolds et al.,³⁰ PM7 D2 is a derivative of the benzodithiophenedione (BDD)-based PM7 donor polymer featuring an ester-functionalized terthiophene group, which was found to be more soluble than PM7 in chlorobenzene due to its flexible backbone conformation and reduced tendency to form semicrystalline fiber aggregates.²⁵ As a result, OSCs fabricated from this donor polymer have been found to be more resilient to different coating temperatures.³⁰ Compared to PM7, we also found that PM7 D2 is soluble in toluene even at 20 mg/mL, whereas PM7 does not dissolve in the same solvent (Figure S2a). Due to its poor solubility, PM7-based devices exhibit an extremely poor performance of 3.1% when blade-coated from toluene solution (Figure S2b), making it difficult to use for green solvent processing. Other high-performing donor polymers, such as D18, are also poorly soluble in toluene due to their highly conjugated backbone.³¹ In contrast, the improved backbone flexibility of the PM7 D2 polymer makes it an excellent model system for studying the impact of the solvent environment on the polymer aggregate structure and morphology. In this study, we thus investigate how varying the solvent-polymer affinity, particularly when transitioning from halogenated to nonhalogenated solvents, impacts the solution aggregate structures of PM7 D2. Figure 1b,c shows the molecular structures of the

small molecule acceptor, ITIC-4F, and a series of halogenated (1-chloronaphthalene - CN and chlorobenzene - CB) and nonhalogenated (toluene - TL and anisole - AN) solvents used in this study, respectively. The color background of Figure 1c indicates that the solvent becomes greener, moving from CN to AN. Larsen and Edman et al. have recently published an online tool³² that provides a quantitative sustainability score (G) for common solvents in printed electronics using the GlaxoSmithKline (GSK) green solvent selection guide. 33-35 Based on this guideline, the G index for CB, TL, and AN are found to be 5.4, 6, and 7.4, respectively, suggesting that AN is the greenest solvent among this series of solvents (G index for CN has not been determined, but it is reported to be more lethal to health compared to CB).6 It is also worth mentioning that AN is a natural product found in plants, Peristeria Elata and Phallus Impudicus, and is even used as a food additive, ³⁶ which is another strong indication of its potential as a useful green solvent to process printed electronic devices.

Conjugated polymers are often poorly dissolved in nonchlorinated or green solvents, making it challenging to obtain uniform thin films. Therefore, determining the solvent quality is a crucial step toward morphology control in green solventprocessed OSCs. We resort to Hansen solubility parameters for the initial estimation of solvent quality, which is based on the "like-dissolves-like" principle and is calculated using a group contribution approach.³⁷ Although it remains in question whether the Hansen solubility theory is applicable to π conjugated systems featuring extensive electron delocalization, recent work has shown that it correlates well with solubility in common solvents due to the dominating impact of dispersion interactions.³⁸ The Hansen solubility method takes three solubility parameters into consideration: (1) dispersion ($\delta_{\rm D}$); (2) polar (δ_P) ; and (3) hydrogen bonding contributions (δ_H) . By using these parameters for polymer (1) and solvent (2), the solubility distance (R_a) , a relative measure of solubility, is then calculated as follows

$$R_a^2 = 4(\delta_{\rm D1} - \delta_{\rm D2})^2 + (\delta_{\rm P1} - \delta_{\rm P2})^2 + (\delta_{\rm H1} - \delta_{\rm H2})^2$$

A low R_a value implies that the polymer has good solubility, thereby exhibiting strong polymer—solvent interactions. In poor solvents with a large R_a value, on the other hand, the polymer polymer interaction is stronger than the polymer-solvent interaction, making it easier to form solution-state aggregates.²⁴ Since the polymer-polymer interaction involves backbonebackbone, side chain-side chain, and side chain-backbone components, it is imperative to compare the quality of solvents for the conjugated backbone and the side chains, respectively. Accordingly, we estimated the solubility distance for the backbone and side chain of the PM7 D2 polymer in these halogenated and green solvents using the group contribution method by van Krevelen and Hoftyzer,³⁹ which uses the individual functional groups or structural elements to estimate the solubility parameters. Using the molecular structures of the conjugated backbone and the alkyl side chain (Figure S3), the solubility distance for each solvent was determined as shown in Figure 1d (details of the solubility parameters are tabulated in Table S2). Due to its fused-ring aromatic core, CN appears to be the best solvent for the conjugated backbone but the poorest solvent for the alkyl-ester side chains. In fact, CN has also been demonstrated to be a poor solvent for alkyl side chains in other conjugated polymer systems, including PII-2T and P(NDI2OD- $T2).^{15}$

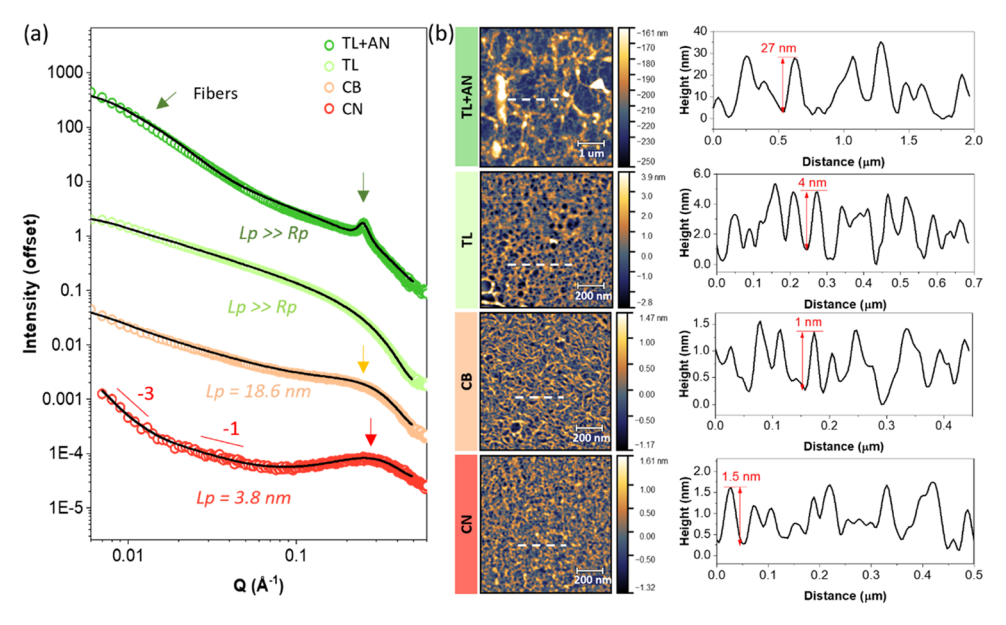


Figure 2. (a) Solution SAXS profiles for PM7 D2 in CN, CB, TL, and TL+AN solvents at 20 mg/mL concentration. (b) AFM height images of the freeze-dried PM7 D2 solutions in the same four solvents and their corresponding height profiles across the dashed lines. The concentration used for freeze-drying is also 20 mg/mL for all solutions.

Moving toward greener solvents, solvent quality decreases toward the conjugated backbone, as evidenced by the increase in the R_a value, which closely aligns with the trend observed in the dispersion contribution ($\delta_{\rm D}$) among the four solvents (Table S2). The δ_D parameter is strongly correlated with the solvation enthalpy of conjugated polymers based on molecular dynamics simulations.³⁸ The fact that halogenated solvents are generally good solvents for the π -conjugated backbone due to their larger van der Waals coefficient of chlorine atoms compared to carbon atoms³⁸ is also consistent with our findings. This result is further confirmed by the UV-vis spectroscopy measurements of these polymer solutions, as shown in Figure 1e. The UV-vis absorption onset of PM7 D2 redshifts from CN to AN, suggesting an increase in the conjugation length or the backbone rigidity due to the decreasing solvent affinity toward the backbone. 40 We note, however, that red shift in the UV-vis spectra can also be related to the solvatochromic effect due to the change in solvent polarity, making it difficult to directly correlate the wavelength shifts to polymer conformation.⁴ Besides the red shift in the absorption onset, a shoulder peak at 585 nm emerges in AN, indicating the formation of ordered aggregates. 42,43 We also observed micrometer-scale large aggregates in PM7 D2 solution in AN under microscopy (Figure S4a), validating that the shoulder peak in the UV-vis is due to aggregation. In TL, a weak shoulder peak is also observed in the UV-vis spectra, implying a small amount of such ordered aggregates. Interestingly, the CN solution seems to have a shoulder peak at 545 nm; however, the location of this peak is at a much lower wavelength compared to the aggregate peak, denoting that it likely originates from vibronic transitions. The energy separation between this shoulder peak and the main absorption of CN solution at 510 nm is 0.16 eV, which lies in the range of 0.14 to 0.18 eV for vibronic progressions. 44,45

Polymer Solution-State Aggregation. To investigate the solution aggregate structures of PM7 D2 in various solvents, we utilized small-angle X-ray scattering (SAXS), which has been widely used to decipher the solution-state aggregate structures of conjugated polymers. ^{25,46–48} Shown in Figure 2a are the 1D

scattering profiles, as well as their model fits of PM7 D2 in four different solvents. Because of the poor solubility of PM7 D2 in AN, we used a mixture of TL and AN solvent with 25 vol % TL content (TL+AN), which dissolved the micrometer-scale aggregates in pure AN (Figure S4b). Based on the scattering profiles, it is clearly observed that PM7 D2 in TL+AN contains two Guinier knees around 0.01 and 0.3 Å⁻¹, which can be attributed to the cross sections of fiber aggregates and single polymer chains, respectively. 25,47 Using the model fitting approach that we previously reported for conjugated polymer solutions containing polymer fibers and single polymer chains, ⁴⁷ the diameter of these fiber aggregates is determined to be \approx 10 nm (Table S3). Further details of fitting the scattering profiles are provided in Supplementary Note 1, which includes the deconvolution of the model fits (Figure S5) and the resulting fitting parameters (Table S3). Notably, the scattering profile of PM7 D2 in TL+AN also contains a crystalline lamellar peak at $0.25 \,\text{Å}^{-1}$, corresponding to a lamellar stacking distance of d_{lamellar} = 2.5 nm. This suggests that the fiber aggregates of PM7 D2 formed in this solvent are semicrystalline.

In comparison to PM7 D2 in TL+AN, the scattering profiles for PM7 D2 in CN, CB, and TL are rather featureless with no Guinier knee at low $Q(Q < 0.03 \text{ Å}^{-1})$ or crystalline lamellar peak at high Q range $(Q > 0.1 \text{ Å}^{-1})$. However, a broad structure factor peak at 0.26 Å^{-1} ($d_{\text{lamellar}} = 2.4 \text{ nm}$) is visible in CN but becomes less apparent in CB and disappears entirely in TL. We attribute this broad structure factor peak to disordered or amorphous lamellar interactions based on its proximity to the crystalline lamellar peak observed in TL+AN. The fact that this broad peak is more obvious in CN but less apparent in CB and completely absent in TL is consistent with the fact that CN is a poor sidechain solvent and that the solubility toward the side chain progressively increases from CN to CB to TL (Figure 1d). Besides the broad structure factor peak, the scattering profile for PM7 D2 in CN contains a Porod region with a slope of -3 at low Q, which represents a fractal or network-like structure, 49,50 confirmed with freeze-dried imaging discussed later. This observation suggests that PM7 D2 forms amorphous network

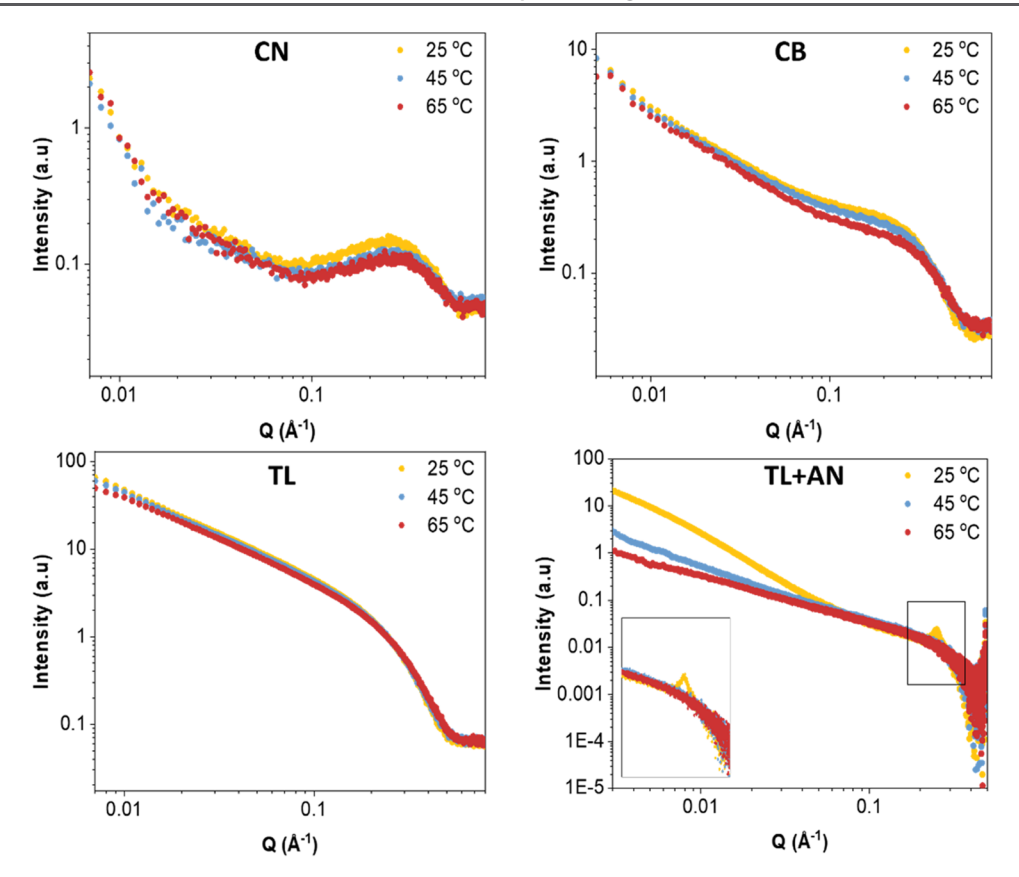


Figure 3. Temperature-dependent SAXS profiles of PM7 D2 in four different solvents. The scattering profile for PM7 D2 in TL+AN changes most drastically with increasing temperatures as compared to the other solutions, as the semicrystalline fiber aggregates dissolve at high temperatures.

aggregates via side-chain associations. At the intermediate region of PM7 D2 in CN, the Porod slope changes from -3 to -1 due to the contribution of rigid polymer chains or chain segments. Compared with PM7 D2 in CN, the scattering profiles of CB and TL are dominated by the Porod region with a slope of -1, indicating that the polymer chains become more rigid. Accordingly, the model fitting results indicate that the persistence length of polymer chains increases from 3.8 nm in CN to 18.7 nm in CB, which is consistent with the decreasing solvent quality toward the conjugated backbone. The persistence lengths of polymer chains in TL and TL+AN cannot be determined accurately due to the slope of -1 being too close to the asymptotic limit for the flexible cylinder model, but they are expected to be highly rigid $(l_p \gg R_p)$.

Although polymer chains become rigid when transitioning to nonhalogenated solvents, the exact nature of aggregates in CB and TL is difficult to determine from SAXS measurements because the low Q region in our SAXS measurements is limited to 0.006 Å^{-1} . It is possible that PM7 D2 exists as fully dispersed, noninteracting polymer chains in these solvents. However, we observe a broad scattering feature around 1.5–1.7 Å⁻¹ (d = 3.8– 4.2 Å) from our wide-angle X-ray scattering (WAXS) measurements (Figure S6a,b), indicative of loose packing of alkyl side chains and/or backbone interactions. In a poor side-chain solvent CN, this WAXS scattering feature has a *d*-spacing of 4.2 Å, consistent with the typical alkyl side-chain stacking distance. 51,52 In contrast, CB and TL solutions have a shorter d-spacing of around 3.8 Å, which is much smaller than the alkyl side-chain stacking distance observed even in crystalline octadecyltrichlorosilane (OTS) films (d = 4.2 Å). Furthermore, considering the weak lamellar stacking of PM7 D2 in CB

and the absence of lamellar stacking in TL, the broad peak near 1.65 Å in the WAXS measurements of CB and TL solutions is attributed to interactions between polymer backbones rather than alkyl side chains. Furthermore, for PM7 D2 in TL+AN, we observe an additional $\pi-\pi$ stacking peak at $d_{\pi-\pi}=3.6$ Å (Figure S6a), which is close to the crystalline $\pi-\pi$ stacking in most conjugated polymer films. Our X-ray scattering measurements thus suggest that PM7 D2 in TL+AN forms semicrystalline fiber aggregates through crystalline lamellar and $\pi-\pi$ stacking, whereas CN forms semiflexible amorphous network aggregates via side-chain associations. Mutual solvents, including CB and TL, on the other hand, lead to rigid amorphous network aggregates via polymer backbone interactions.

To complement our SAXS results, we further conducted atomic force microscopy (AFM) imaging on the freeze-dried solutions, as shown in Figure 2b. Freeze-drying is an effective technique to preserve the solution-state aggregates by rapidly quenching the solutions using cryogens (i.e., liquid ethane), which has been applied to deciphering the solution aggregate structures of conjugated polymers in previous studies. 25,47,53,54 Based on AFM imaging on the freeze-dried samples, fiber aggregates with thicknesses of around 20-30 nm were observed in TL+AN, as shown in Figure 2b. This result is larger than the diameter of 10 nm obtained from SAXS fitting, which could be due to the polydispersity of these polymer fibers and the instrument limitation of SAXS. Compared to TL+AN, no largescale aggregates are observed in all other solutions; instead, small polymer network-like aggregates can be seen in AFM height imaging. These networks are likely comprised of single polymer chains since the height profiles indicate thicknesses less than 5 nm. For CB and CN, the thickness of the network aggregates is

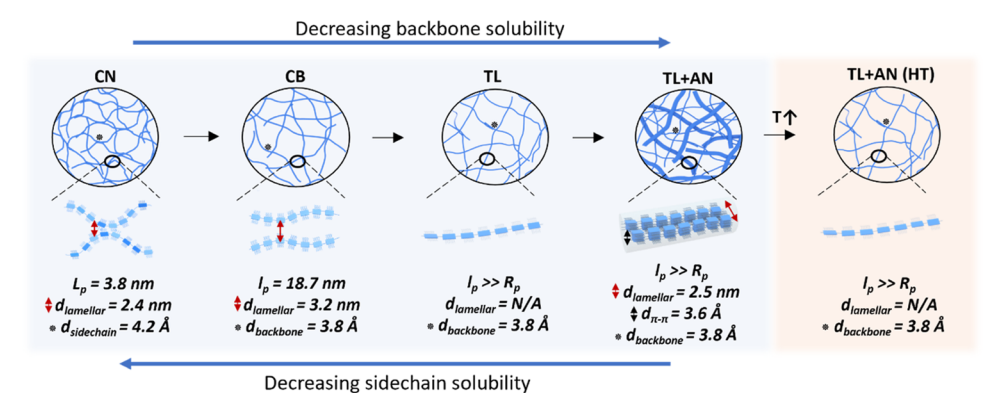


Figure 4. Schematic illustration of the solution-state aggregates depending on the solvent and solution temperature. Transitioning from halogenated to nonhalogenated solvents decreases the backbone solubility, which causes the polymer aggregate structure to transition from amorphous networks with strong side-chain associations (CN) to semicrystalline fiber aggregates (TL+AN). In solvents where the side-chain and backbone solubility are balanced (CB and TL), the polymer also forms amorphous network aggregates but mainly through backbone interactions rather than side-chain associations compared to the CN case. Similar amorphous network aggregates are also obtained by increasing the solution temperature of TL+AN, which leads to an order-to-disorder transition of semicrystalline fiber aggregates. Solution-state aggregate structures at high solution temperatures of CN, CB, and TL are not shown since the structure does not change with the increasing solution temperature.

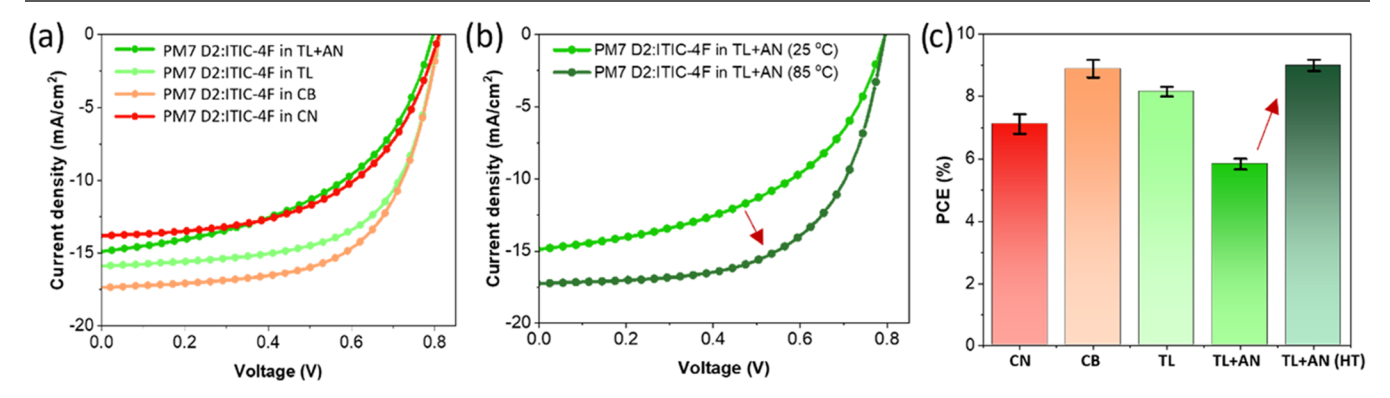


Figure 5. (a) Current density and voltage (JV) characteristic curve for PM7 D2:ITIC-4F-based devices blade-coated from various solvents; (b) those cast from the TL+AN mixture solvent at room temperature and 88 °C, which will be referred to as high temperature (HT). (c) Comparison of the power conversion efficiencies for the devices in (a) and (b). All devices are fabricated and tested under ambient or glovebox-free conditions.

only 1–1.5 nm, a strong indication that the network aggregates are comprised of single polymer chains. For TL, the width of these aggregates is around 4 nm, somewhat larger than those observed in CB and CN. This could be correlated with more extended/solubilized side chains and/or the absence of sidechain associations for holding together a tight network of polymer chains resulting in polymer chains being overlapped during the freeze-drying process. In contrast, the network aggregates of CN are more compact, likely due to the strong side-chain associations, which agrees with the more intense structure factor peak observed in the scattering profile.

We have previously demonstrated that the donor polymer, PM7, forms semicrystalline fiber aggregates that are sensitive to solution temperature. Notably, the fiber aggregates of PM7 D2 formed in TL+AN also depend strongly on temperature, as evidenced by our temperature-dependent SAXS (Figure 3). With increasing solution temperature, the Guinier region corresponding to the fiber aggregates and the crystalline lamellar stacking peaks completely disappear, suggesting the dissolution of these aggregates. As the fiber aggregates dissolve at high temperatures, the crystalline π – π stacking peak also disappears based on the temperature-dependent WAXS measurements (Figure S6c). Nevertheless, the broad scattering feature at d = 3.8 Å, corresponding to amorphous backbone interactions between polymer chains, remains at high temperatures. This

observation suggests that the TL+AN sample at high temperatures is composed of rigid amorphous network aggregates resembling those found in PM7 D2 in TL and CB. It is interesting to note that compared to previous studies where temperature-dependent aggregation has been correlated to molecular design, ^{55,56} our findings reveal that temperature-dependent aggregation is a more general behavior that is dependent on polymer—solvent interactions. Compared to TL +AN, all other solutions are less dependent on the solution temperature, only leading to a decrease in the scattering intensity, which is consistent with the absence of semicrystalline fiber aggregates in these solutions.

Figure 4 depicts the schematics of the solution-state aggregates as a function of solvent and solution temperature based on our X-ray scattering and freeze-dried imaging results. In the poor side-chain solvent CN, PM7 D2 forms semiflexible amorphous network aggregates with strong lamellar and side-chain interactions ($d_{\text{lamellar}} = 2.4 \text{ nm}$ and $d_{\text{side chain}} = 4.2 \text{ Å}$), whereas in a poor backbone solvent (TL+AN), the polymer chains become more rigid, eventually forming semicrystalline fiber aggregates in TL+AN with crystalline lamellar ($d_{\text{lamellar}} = 2.5 \text{ nm}$) and $\pi - \pi$ stacking ($d_{\pi - \pi} = 3.6 \text{ Å}$). In mutual solvents (CB and TL), PM7 D2 forms rigid amorphous network aggregates mainly through polymer backbone associations ($d_{\text{backbone}} = 3.8 \text{ Å}$) with weak ($d_{\text{lamellar}} = 3.2 \text{ nm}$) or no lamellar

Table 1. Photovoltaic Parameters of PM7 D2:ITIC-4F-Based OSCs Blade-Coated from Different Solvents under an Illumination of Air Mass 1.5 Global (AM 1.5G) at 100 mW/cm²

samples	coating temperature (°C)	PCE (%)	FF (%)	$J_{\rm sc}$ (mA/cm ²)	$V_{\rm OC}$ (V)
CN	122	7.1 ± 0.3	56.6 ± 1.6	15.3 ± 0.8	0.82 ± 0.01
CB	25	8.9 ± 0.3	62.7 ± 1.2	17.4 ± 1.2	0.82 ± 0.01
TL	25	8.2 ± 0.2	63.2 ± 0.9	15.9 ± 0.1	0.81 ± 0.01
TL+AN	25	5.8 ± 0.2	49.3 ± 0.9	14.9 ± 0.1	0.80 ± 0.01
TL+AN (HT)	88	9.0 ± 0.2	68.8 ± 0.4	16.4 ± 0.3	0.80 ± 0.01

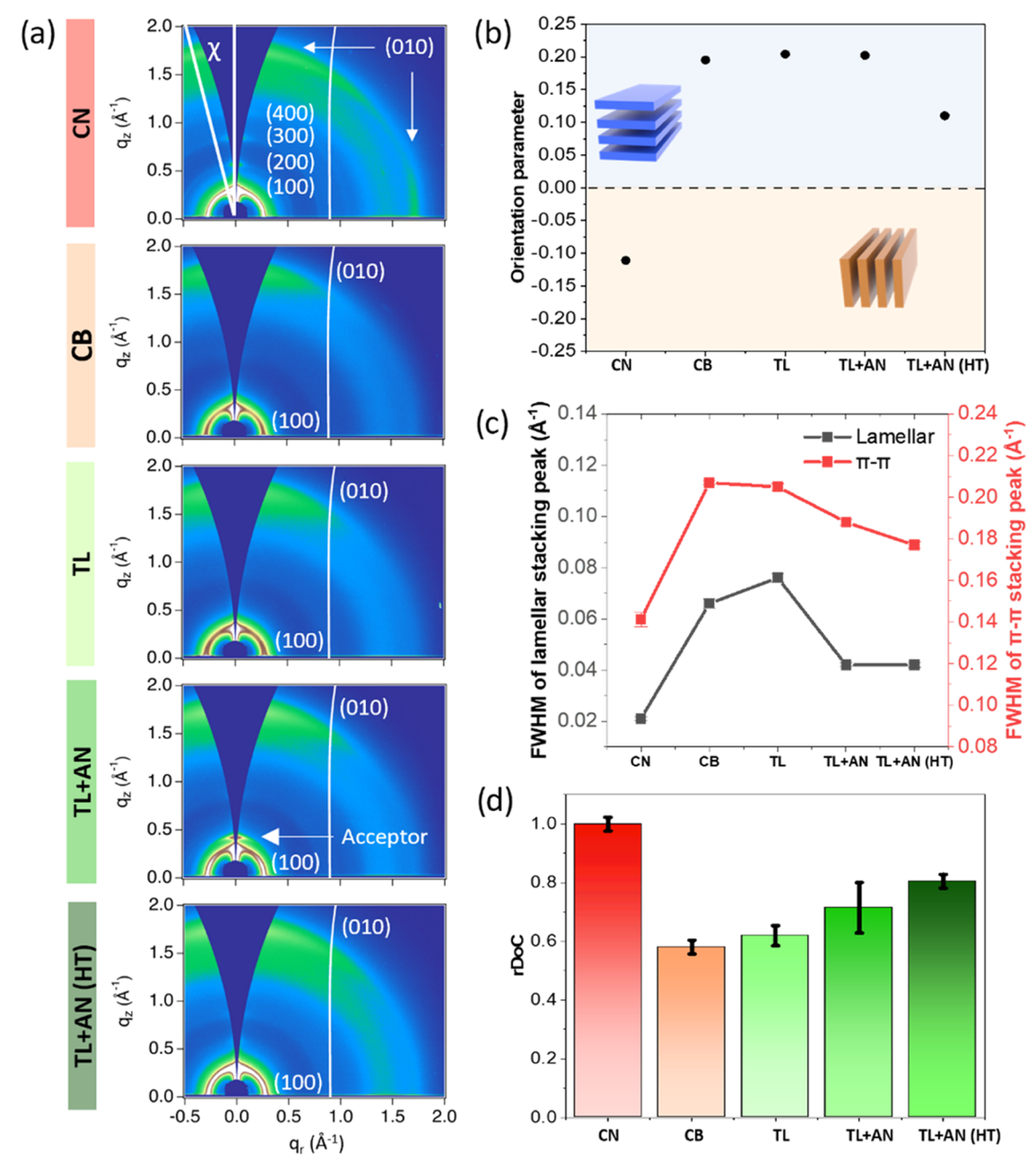


Figure 6. (a) 2D GIWAXS patterns of PM7 D2:ITIC-4F blend films. (b) Comparison of Herman's orientation parameter where more negative value corresponds to edge-on population; (c) fwhm of (010) and (100) peaks from the GIWAXS patterns. (d) Comparison of the relative degree of crystallinity (rDoC) of blend films cast from different solvents.

stacking. Rigid amorphous network aggregates, resembling those in CB and TL, are also obtained from semicrystalline fiber aggregates when increasing the solution temperature of TL +AN.

Device Performance Characterizations. We subsequently investigated how these distinct solution-state aggregates of PM7 D2 impact the device performance of the OSCs. Using the inverted (ITO/ZnO/PM7 D2:ITIC-4F/MoO₃/Ag) architecture, we fabricated BHJ-based OSCs, in which the photo-

active layer was blade-coated from a blend solution of PM7 D2:ITIC-4F (1:1) under ambient conditions without additives for relevance to industrial manufacturing of OSCs. All other fabrication steps and device testing were also conducted under glovebox-free or ambient conditions. Figure 5a shows the comparison of the current density (J_{sc}) as a function of voltage (V) depending on the casting solvent with the device parameters provided in Table 1, which also includes the coating temperatures used for blade coating. In all cases except for CN, room temperature (25 °C) was selected as the coating temperature, whereas in CN, a coating temperature of 122 °C was selected due to its high boiling point. At these coating temperatures, the vapor pressures of all solvents are matched to ensure similar drying times, except for TL (Table S4). Due to the high volatility of TL, the coating temperature had to be decreased much lower than room temperature to match the vapor pressures of the other solvents, which was impractical due to considerations such as water condensation at low temperatures. For the TL+AN mixed solvent, we note that the drying kinetics becomes more complicated than a single solvent system due to the different boiling points of TL and AN. Although the vapor pressure of the initial TL+AN mixture matches that of CB at room temperature (Table S4), TL has a lower boiling point than AN, resulting in an increased volume fraction of AN later in the drying stage and thus overall slower drying kinetics. However, we show that devices cast from CB and TL do not depend significantly on the coating temperatures, as the film thickness is matched by varying the coating speed (Figure S7). This implies that drying time differences arising from unmatched vapor pressures likely have minimal impact on the performance of devices cast from TL and TL+AN.

When comparing the device parameters as shown in Figure 5a and Table 1, it is apparent that the intermediate solvents, CB and TL, yield higher efficiencies compared to the two extreme cases when either backbone-selective (CN) or side-chain-selective (TL+AN) solvents are used. This result implies that forming rigid amorphous network aggregates with weak or no side-chain interactions by balancing the solubility of the polymer backbone and side chains is critical for optimizing the device performance of OSCs. Besides using mutual solvents, these rigid amorphous aggregates can also be formed from semicrystalline fiber aggregates when the solution temperature is increased (Figure 4). Accordingly, when we fabricate devices at high coating temperatures (HT), devices cast from TL+AN yielded a drastic enhancement in performance from 5.8 to 9.0% (Figure 5b,c). On the other hand, devices cast from CB and TL showed minimal dependence on the coating temperatures, consistent with the relative stability of PM7 D2 aggregates depending on the solution temperature as compared to TL+AN (Figure S7 due to the high boiling point of CN and instrument limitations, CN-based devices are not fabricated at temperatures higher than 122 °C). Nevertheless, it is important to highlight that a slight improvement in PCE was observed with an increase in the coating temperature, especially when CB was employed (Figure S7). This implies that coating temperature and/or drying kinetics have a minimal but non-negligible effect on the device performance, likely inducing changes in the blend film morphology.⁵⁷ In contrast to CB and TL, TL+AN devices exhibit a strong coating temperature dependence, which can be primarily attributed to the structural transition of semicrystalline fiber aggregates to form rigid amorphous network aggregates at high temperatures. We also note that this result closely aligns with our previous report, where semicrystalline fiber aggregates

of the PM7 polymer formed in CB lead to a substantial enhancement in OSC performance from 5.8 to 8.7% as these aggregates form amorphous network aggregates during hot solution processing.²⁵

Flim Morphology Characterizations. As shown in Table 1, the differences in the device efficiencies are mainly due to the large short circuit current (J_{sc}) and fill factor (FF), which depend on the blend film morphology. 58 Therefore, to better understand the trend observed in the device performance of OSCs, we studied the morphology of the blend films using various X-ray diffraction methods, including grazing-incidence-wide-angle Xray scattering (GIWAXS), resonant soft X-ray scattering (RSoXS), and complementary imaging techniques, including photoinduced force microscopy (PiFM) and conductive AFM (c-AFM). Figure 6a shows the 2D scattering patterns of the blend films obtained from GIWAXS measurements. The scattering patterns and linecut profiles for the neat donor and acceptor films are provided in Figures S8 and S9. Both neat donor polymer and blend films exhibit in-plane and out-of-plane (010) peaks, corresponding to $\pi - \pi$ stacking distance around q =3.6 Å, determined from the linecut profiles (Figure S10). Notably, this distance is the same as the π - π stacking distance observed in the fiber aggregates in the TL+AN solution. However, the ITIC-4F acceptor barely shows any (010) peak (Figure S9), suggesting that the π – π stacking peaks observed in the blend films arise largely from the crystallization of the donor polymer. When comparing the scattering patterns, it is evident that the blend film cast from CN exhibits a strong in-plane (010) peak, which corresponds to edge-on polymer orientation in the crystalline domains. To better compare the distribution of molecular orientation in these blend films, partial pole figures were obtained (Figure S11a) using approaches previously reported. 59-62 These pole figures are constructed by plotting the intensity of the (010) peak from 5° sector cut profiles from the scattering patterns within the range of $10^{\circ} < \chi < 80^{\circ}$, where χ = 0° corresponds to the out-of-plane direction. The peak intensities are then normalized to the 0-1 scale for direct comparison of the molecular orientations across different films. Based on these pole figures, a sharp increase in the intensity of the (010) peak at higher χ angles is observed for the blend film cast from CN, which is more drastic compared to other films.

We further estimated Herman's orientation parameter $(S)^{63,64}$ based on the distribution of the (010) peak using the sample normal as the director as shown in Figure 6b. The S parameter ranges from -0.5 to 1, corresponding to a complete edge-on to face-on population when the azimuthal angle is selected along the surface normal. Figure 6b clearly shows that the S parameter is more negative for CN compared with the other films, which is a clear indication of predominantly edge-on molecular orientation in the crystalline domains. Interestingly, we found that the orientation parameter is significantly more negative at the air-liquid interface for the CN case (Figure S11b). Therefore, we attribute the edge-on preferred molecular orientation in CN to the unfavorable side-chain and solvent interactions of PM7 D2 and CN, causing the side chains to orient toward air. Compared to the blend film cast from CN, other films yield preferential face-on orientation, which is evident from their positive S parameters. Since edge-on orientation is often unfavorable for charge transport in OSCs, the fact that devices cast from CN yield poorer performance is not surprising. However, molecular orientation does not seem to be the main reason for the poor performance in devices cast from TL+AN at room temperature, given that the orientation is

mainly face-on, which is expected to favor charge transport in OSCs

To compare the crystallinity of the blend films, we determined the full width at half-maximum (fwhm) of the (010) and (100) peaks and the relative degree of crystallinity of the blend films using GIWAXS measurements as shown in Figure 6c,d, respectively. Based on Figure 6c, the fwhm of both (010) and (100) peaks are much smaller in CN and TL+AN films than in CB and TL, suggesting larger crystal sizes and/or lower paracrystalline disorder⁶⁵ compared to the films cast from CB and TL. In CN, high-order lamellar peaks are also clearly visible compared to other films, suggesting its long-range crystalline order. We also calculated the relative degree of crystallinity (rDoC) by integrating the geometrically corrected (010) peak intensities over χ following the protocols of previous reports. 59,66 Figure 6d shows the comparison of rDoC in these blend films, suggestive of the higher crystallinity of PM7 D2 cast from CN and TL+AN solvents compared with CB and TL.

To understand why CN and TL+AN yield more crystalline films than CB and TL, we first investigated the assembly pathways of PM7 D2 using cross-polarized optical microscopy (CPOM). As we increase the solution concentration to 200 mg/ mL using the drop and drying method (see Experimental Methods for details), we observe the emergence of lyotropic liquid crystalline (LC) phases in CB, TL, and TL+AN, with TL +AN more readily forming LC phases even at 60 mg/mL (Figure S12). In CN, PM7 D2 shows some birefringence at the edge of the solution at 200 mg/mL, although the bulk of the solution is still mainly isotropic. This observation aligns with previous findings suggesting that poor backbone solvents are more likely to induce the lyotropic LC phase.⁶⁷ On the other hand, we observe that semiflexible amorphous network aggregates, particularly those formed in CN, delay the formation of LC phases. Given that CN does not readily crystallize or form an LC phase even at 200 mg/mL, it is surprising that the blend film is more crystalline than other films based on our GIWAXS results. Investigating the crystallization mechanism of PM7 D2 in CN using in situ CPOM measurement (Supplementary v 1) reveals direct crystallization of PM7 D2, similar to the crystallization of the PII-2T polymer in CN as previously reported.²⁹ We thus attribute the pronounced crystallization of PM7 D2 in CN to the strong side-chain interactions within these amorphous network aggregates caused by the poor solvent quality of CN toward the side chains. We also note that the top and bottom surface of the dried film of PM7 D2 in CN show different birefringence under CPOM (Figure S13), consistent with the different molecular orientation at the interface (edgeon) versus in the bulk of the film (face-on).

In contrast to CN, where PM7 D2 undergoes direct crystallization, the higher crystallinity of PM7 D2 in TL+AN could be attributed to its tendency to form an LC phase (Figure S12). However, our findings suggest that LC phase formation is suppressed when the film is blade-coated in the Landau—Levich (LL) regime, highlighting the importance of coating regimes on the assembly pathway of conjugated polymers. To demonstrate this, we compared the assembly pathways of PM7 D2 under the evaporation regime vs the Landau—Levich (LL) regime. When the films were coated in the evaporation regime at low coating speeds, all films were highly birefringent under CPOM (Figure S14), implying that the crystallization process undergoes an LC-mediated assembly pathway. However, coating in the evaporation regime led to highly nonuniform films due to the stick and slip effect, opposition of the prompting us to choose

the LL regime for OSC fabrication. When PM7 D2 solution in TL+AN was printed in the LL regime, however, we did not observe any LC phase formation during the coating process under CPOM imaging (Supplementary Video 2). Typically, crystallization mediated by the LC phase shows highly birefringent features at the triple-phase contact line before crystallization.^{61,68} Figure S14 also shows that all films become less birefringent and thus more isotropic in the LL regime compared to those coated in the evaporation regime at very low coating speeds, indicating that the LC mesophase is suppressed to result in the direct crystallization pathway. Therefore, we attribute the improved crystallinity of PM7 D2 cast from TL +AN to the direct crystallization of the pre-existing crystalline fibers rather than the LC-mediated crystallization. As shown in Figure 6a, we also observe an out-of-plane peak near 0.4 Å^{-1} , which is not observed in any other blend films. Based on the neat acceptor GIWAXS patterns, we attribute this peak to the ITIC-4F acceptor (Figure S9c). The fact that this peak is more pronounced in the TL+AN solvent seems to suggest that the semicrystalline fiber aggregates also enhance the crystallization of ITIC-4F. It is also worth noting that even at an elevated temperature of 88 °C, the film cast from TL+AN (HT) retains its crystallinity (Figure 6c,d) even though the fiber aggregates dissolve at high temperatures. This suggests that PM7 D2 still maintains its strong tendency to crystallize in TL+AN due to the reduced nucleation barrier in a poor solvent.71

Since PM7 D2 undergoes direct crystallization in TL+AN when coated in the LL regime, it also implies that CB and TL lead to direct crystallization of PM7 D2 since CB and TL are less conducive to the LC phase (Figure S12). The film crystallinity of PM7 D2 in CB and TL, however, is lower compared to TL+AN, which is attributed to the formation of rigid amorphous network aggregates of PM7 D2 in CB and TL solutions that delay the formation of crystalline fiber aggregates during drying, thereby preventing strong crystallization of PM7 D2. The lower crystallinity of CB and TL films compared to CN is also attributed to the rigid amorphous network aggregates of PM7 D2 in CB and TL. Unlike the flexible amorphous aggregates of PM7 D2 with strong side-chain associations in CN, these rigid amorphous network aggregates only possess weak or no sidechain associations, which prevent strong crystallization at the air-liquid interface. Furthermore, the rigid amorphous network aggregates likely undergo crystallization through backbone ordering rather than side-chain ordering, which could contribute to increased nucleation density and small crystal sizes in the solid state.15

To sum up, although PM7 D2 can form an LC phase in all solvent systems at high solution concentrations, we found that coating films in the LL regime suppress the formation of the LC phase, even in TL+AN, which readily forms the LC phase. Ultimately, PM7 D2 undergoes direct crystallization in all solvents, where the structure of the solution aggregates tuned the film crystallinity. In CN, semiflexible amorphous network aggregates led to strong crystallization driven by their strong side-chain associations at the air—liquid interface. Similarly, semicrystalline fiber aggregates formed in TL+AN also led to high film crystallinity by acting as the seed crystallites (e.g., heterogeneous crystallization). On the other hand, rigid amorphous network aggregates formed in CB and TL led to reduced film crystallinity owing to the more balanced side-chain and backbone solubility.

Besides the crystallinity and molecular orientation, the phaseseparated structure of the photoactive layer is crucial for charge

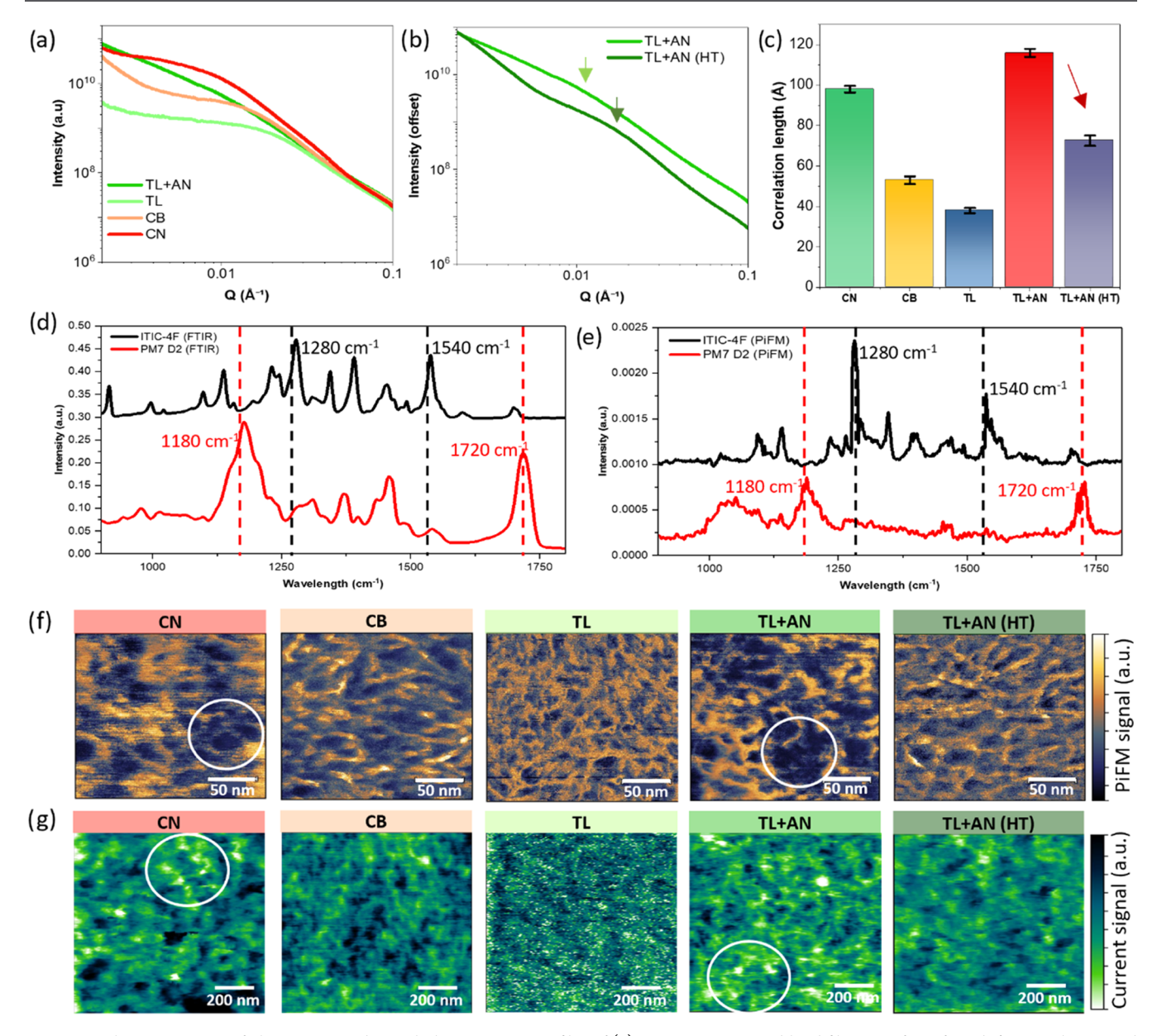


Figure 7. Characterization of phase-separated morphology. RSoXS profiles of (a) PM7 D2:ITIC-4F blend films cast from four different solvents and (b) those cast from TL+AN at 25 °C and high coating temperatures (HT) at 88 °C. (c) Correlation lengths of blend films based on DAB model fitting. (d) Bulk FTIR measurement results for PM7 D2 and ITIC-4F materials. (e) Surface PiFM measurements on PM7 D2 and ITIC-4F neat films blade-coated from CB. (f) PiFM imaging results for the blend films when using the IR laser tuned at 1280 cm⁻¹, where the circled regions correspond to the donor-rich domains. (g) c-AFM images of the blend films using a bias voltage of +3 V, where the circled regions correspond to the donor-rich domains.

generation in organic solar cells. To quantify the domain sizes in the blend films, we used resonant soft X-ray scattering (RSoXS), which uses X-ray energies near the aromatic C 1s $\rightarrow \pi^*$ to enhance the contrast between the donor and acceptor materials. As previously reported, the scattering contrast, however, not only originates from material contrast but also includes contributions from molecular orientation and surface roughness. To Based on our previous study, the surface roughness contribution is negligible for the PM7 D2:ITIC-4F system, but molecular orientation contribution in this case cannot be easily separated from material contrast. This suggests that scattering features from RSoXS originate from both material and orientation contrasts. Figure 7a,b shows the RSoXS scattering profiles obtained at 284.8 eV for blend films cast from different solvents and films cast from TL+AN at different temperatures.

Based on Figure 7a, the scattering features for CN and TL+AN are located at the lower Q range, corresponding to a larger length scale, which is consistent with their high crystallinity. When coating PM7 D2 in TL+AN at a high coating temperature, on the other hand, the scattering feature shifts toward the higher Q range or smaller length scale (Figure 7b). Using the Debye–Anderson–Brumberger (DAB) model for randomly distributed two-phase systems to fit the scattering profiles,⁷⁴ we estimated the correlation length or spacing between the donor and acceptor materials, as shown in Figure 7c. This figure clearly shows that CN and TL+AN lead to larger correlation lengths compared to those of CB, TL, or TL+AN (HT).

Since the scattering features from RSoXS involve contributions from molecular orientation, we utilized PiFM as a complementary technique to compare the phase-separated

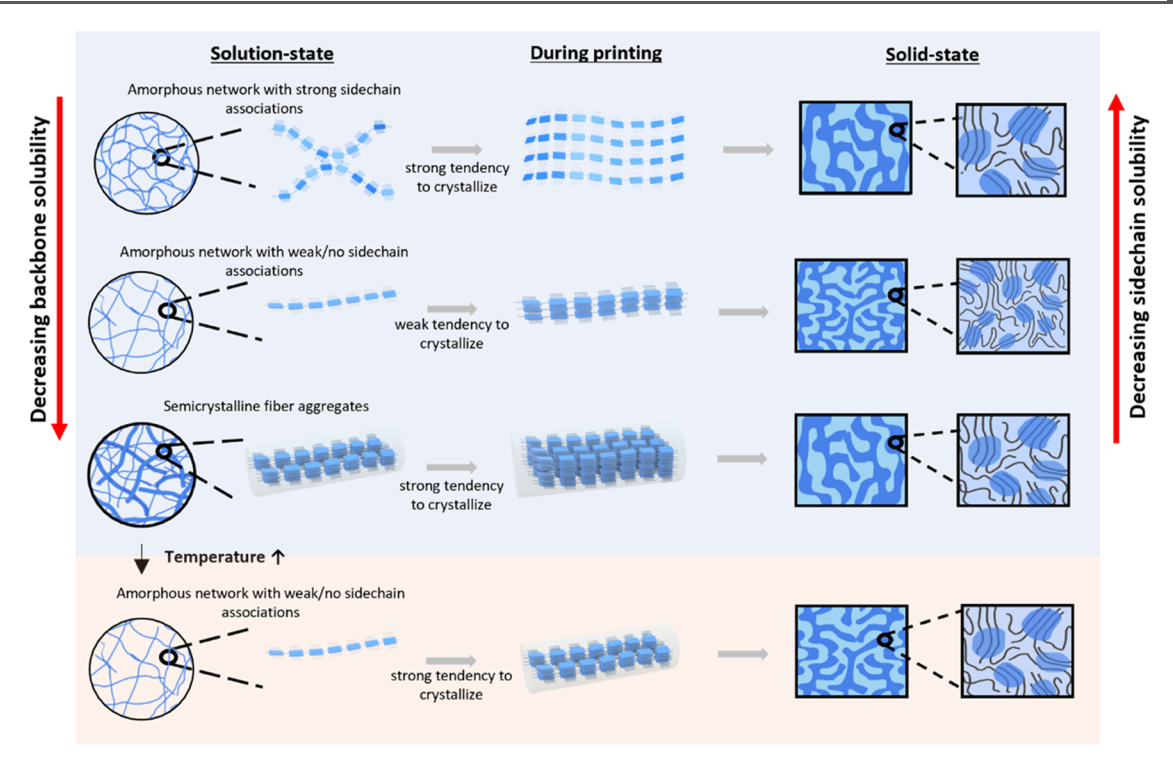


Figure 8. Overall schematics of the assembly pathways for PM7 D2 during OSC processing, depending on the solvent and coating temperature. Poor backbone and side-chain solubility lead to semicrystalline fiber aggregates and amorphous networks with strong side-chain associations, respectively, both resulting in excessive crystallization and large domain sizes. Balancing the backbone and side-chain solubility, on the other hand, forms amorphous network aggregates with weak or no side-chain associations, yielding the most favorable blend morphology with small crystalline domains.

structure of the blend films. PiFM is a scanning probe technique that combines AFM with a tunable infrared (IR) laser to impart chemical contrast, and it has only recently been used to investigate the blend film morphology of OSCs.^{2,75-77} During the PiFM measurement, the IR laser is focused on the region of the sample that interacts with the AFM probe, inducing an electric dipole from the sample, which then creates a mirror dipole on the AFM tip. 76 The dipole—dipole attractive forces between the sample and the tip then create a compositional map of the blend film at 10 nm resolution. Figure 7d,e shows the IR spectra of PM7 D2 and ITIC-4F films obtained from Fourier Transform Infrared (FTIR) for the bulk and PiFM for the sample surface, respectively. Both FTIR and PiFM spectra match very well; particularly, the major peaks at 1280 and 1540 cm⁻¹ for ITIC-4F and 1180 and 1720 cm⁻¹ for PM7 D2 are clearly observed in both FTIR and PiFM. The IR excitation wavelength was then tuned to 1280 cm⁻¹ to image the blend films, as shown in Figure 7f. We note, however, that it was difficult to selectively map the donor-rich regions due to the poor absorption of the donor material in the blend films, even at peak wavelengths 1180 and 1720 cm⁻¹. Nonetheless, the dark regions in Figure 7f can be attributed to the donor-rich domains, which clearly show that PM7 D2 forms large domains when cast from CN and TL+AN compared to those in CB, TL, and TL +AN (HT), consistent with our RSoXS results.

Since the donor domains could not be selectively mapped with PiFM, we also employed c-AFM to map the PM7 D2 domains, as shown in Figure 7g. Using high-work function top and bottom electrodes (PEDOT:PSS for hole transporting layer and Au probe), we were able to map the hole-only transport or donor regions in the blend films. The bright regions in Figure 7g thus show regions with high current due to hole transport, which correspond to PM7 D2 domains. Although the

resolution of the images is lower compared to PiFM, we were able to observe large polymer domains in CN and TL+AN, which is consistent with PiFM imaging. Overall, it is worth noting that our RSoXS, PiFM, and c-AFM results are strongly correlated with the trend observed in the device performance results (Figure 5c), suggesting the importance of domain sizes on OSC performance. It is also generally observed that the more crystalline films tend to form larger domains in blend films, except for TL+AN (HT), which still retained its crystallinity while forming relatively small domains in the blend film. This result could be attributed to the temperature-dependent aggregation behavior of PM7 D2 in TL+AN. It is consistent with previous reports that conjugated donor polymers with temperature-dependent aggregation enable morphology control by processing at elevated temperatures, leading to highly crystalline films with desirable domain sizes. 45,55,80

The assembly pathways of PM7 D2, as inferred from our solution and film characterization results, are illustrated in Figure 8. The schematics portray the relationship between solvent quality, the structure of polymer aggregates, and their crystallization pathways. As solvent affinity decreases toward the conjugated backbone while increasing toward the side chains, the structure of polymer aggregates transitions from semiflexible amorphous networks to rigid amorphous networks and semicrystalline fibers. A Goldilocks effect is exhibited, featuring rigid amorphous network aggregates with weak or no side-chain association, which is the most conducive to favorable morphology for BHJ organic solar cells. During the coating process, both fiber aggregates and semiflexible amorphous networks with strong side-chain interactions showed a greater propensity to crystallize, resulting in blend films with large domains and high crystallinity. When the solvent quality is intermediate for both the backbone and the side chains, rigid

amorphous network aggregates with weak or no side-chain interactions form to prevent excessive crystallization, reducing the domain sizes in the blend film. These rigid amorphous network aggregates can also be achieved from the semicrystalline fiber aggregates by simply raising the solution temperature, resulting in a small phase-separated morphology. Notably, even after the dissolution of fiber aggregates at high temperatures, crystallinity can be maintained while yielding small domain sizes, which is attributed to the temperature-dependent aggregation behavior of PM7 D2 in TL+AN.

CONCLUSIONS

In summary, using PM7 D2 as our model system, along with a series of halogenated and nonhalogenated solvents, we demonstrated that the backbone and side-chain solubility of conjugated polymers plays the key role in determining the structure of polymer aggregates in solution, their assembly pathways, and the blend film morphology. We found that the solvent affinity toward the conjugated backbone decreased while it increased for the side chains when transitioning from halogenated to nonhalogenated solvents. As a result, we obtained three distinct conjugated polymer aggregate structures for PM7 D2 depending on the solvent properties: semiflexible amorphous networks in a poor side-chain solvent, rigid amorphous networks in mutual solvents, and semicrystalline fiber aggregates in a poor backbone solvent. During solution processing, the semicrystalline fiber aggregates acted as nucleation seeds to promote crystallization, leading to large crystalline domains that are detrimental to the OSC performance. Similarly, semiflexible amorphous network aggregates also led to excessive crystallization via crystallization at the air—liquid interface. On the other hand, rigid amorphous network aggregates with weak to no side-chain interactions led to the most favorable blend film morphology owing to the balanced crystallization of PM7 D2, yielding small domain sizes. The rigid amorphous network aggregates were also achieved when increasing the temperature of a poor backbone solvent. Efficient green solvent-processed OSCs were thus enabled by tuning the solution aggregate structures using hot solution processing, which substantially improved the device performance from 5.8 to 9%. Our findings also revealed that despite PM7 D2's ability to form an LC mesophase at high solution concentrations, coating the films in the LL regime suppressed the LC mesophase formation. Instead, direct crystallization pathways were observed in all cases where crystallization of the conjugated polymer strongly depended on the solution aggregate structures. Through this work, we highlight the importance of balancing the backbone and side-chain solubility of conjugated polymers to achieve favorable blend film morphology for the fabrication of efficient OSCs.

EXPERIMENTAL METHODS

Materials. PM7 D2 was synthesized based on the synthesis procedures outlined in the study by Jones and Reynolds et al.,³⁰ with the corresponding molecular weight and dispersity results provided in Table S1. The molecular acceptor, ITIC-4F (purity >99%), was purchased from Brilliant Matters.

UV–Vis Spectroscopy. UV–vis (Cary 60 UV–Vis, Agilent) spectroscopy was used to measure the absorbance of 20 mg/mL polymer solutions of PM7 D2 in a short path length of $10\,\mu m$ quartz cell (Starna Cells). Before each solution measurement, a blank solvent measurement was taken for background subtraction.

SAXS Measurement. SAXS experiments were performed at the 16-ID beamline of the National Synchrotron Light Source II at

Brookhaven National Laboratory to probe the Q ranges of 0.006 < Q $<3~\mbox{Å}^{-1}$ using multiple Pilatus detectors. 81 The samples were measured using a 1.5 mm diameter quartz capillary and custom-made flat sample cells made of 100 µm ultrathin glass windows from Schott AG. Before solution scattering measurements were performed, both empty cells and blank solvents were measured for proper background subtraction. For each measurement, 10-20 repeated measurements were taken on various parts of the sample using X-ray energy at 13.5 keV with a 1 s exposure time to avoid beam damage. The scattering profiles were then obtained by averaging the repeated measurements and subtracting the empty cell and blank solvent contributions using a Python package py4xs in Jupyter Notebooks. 82 The model fitting of the scattering profiles was performed using the SasView program with dI data for weighting, Levenberg-Marquardt with 200 steps for the algorithm where the uncertainties are determined from the covariance matrix, and χ^2 values and the residuals plot were used as the goodness of fit metrics.

Freeze-Drying Method for Imaging the Solution-State Aggregates. Freeze-drying experiments were conducted to image the structure of aggregates in solution by using AFM. The freeze-drying process involves rapid freezing of polymer solutions in a liquid ethane and propane mixture (63% propane and 37% ethane) with a melting point followed by liquid nitrogen storage. The purpose of using the liquid ethane mixture is to ensure rapid freezing of the solution due to its large heat capacity and to prevent polymer aggregation during the cooling process. The resulting frozen polymer solution is then quickly transferred to a Linkam stage at −120 °C under vacuum. The Linkam stage temperature is then slowly increased at a rate of 0.5 $^{\circ}\text{C/min}$ to -80 °C (far below the melting point of chlorobenzene solvent mp = -45 °C and 1-chloronaphthalene mp = -20 °C), followed by 6-8 h of constant monitoring with cross-polarized microscopy to ensure sublimation of all solvents. For TL and TL+AN solvents, liquid nitrogen (bp = -195.8 °C) was used to freeze the solutions due to the low freezing points of TL and TL+AN (mp = -95 °C). The samples were then transferred to the Linkam stage at -135 °C, which was then slowly increased at a rate of 0.5 °C/min to −100 °C, followed by over 12 h of solvent sublimation. The freeze-dried samples were then imaged by the Cypher AFM from Asylum Research using tapping mode.

Device Fabrication. OSCs were fabricated by using the inverted architecture (glass/ITO/ZnO/polymer: ITIC:4F/MoO₃/Ag). Before film deposition, 20 cm × 15 cm ITO-patterned glass substrates (Ossila, Inc.) were cleaned by sonicating sequentially with water, acetone, and finally 2-propanol for 10 min each. The cleaned substrates were then dried with nitrogen and plasma treated (Harrick Plasma PDC-001-HP) for 6 min in 300 mT dry air and high power (30 W). To deposit the electron transporting layer, ZnO solution was prepared by dissolving 1 g of zinc acetate dihydrate (Sigma-Aldrich) and 0.28 g of ethanolamine (Sigma-Aldrich) in 10 mL of 2-methoxyethanol (Sigma-Aldrich) under vigorous stirring for over 12 h in air. This solution was then filtered with a 0.45 μ m PTFE syringe filter before deposition. The filtered solution was deposited on the cleaned ITO substrates by spin-coating for 30 s at 3000 rpm in an ambient atmosphere, which resulted in an active layer thickness of ≈20 to 30 nm measured by a Bruker Dektak XT profilometer. After spin-coating, the ZnO layer was annealed in air at 150 °C for 30 min, followed by slow cooling to room temperature for active layer deposition. The photoactive layer solution for all devices was prepared by dissolving the polymer and ITIC-4F (Sigma-Aldrich) at a 1:1 (w/w) ratio in CN, CB, TL, and TL+AN without any additives. The resulting blend solution was stirred at 40 °C overnight, brought to room temperature, and stirred for at least 12 h before deposition before blade coating. The blend solutions were then blade-coated using a blade angle of 7° and a solution volume of 3 μ L. The conditions used for coating from each solvent are provided in Tables S4 and S5. The film thickness corresponding to these optimal coating conditions was ~80 nm. After blade coating, all films were thermally annealed at 100 °C for 10 min in air before thermal evaporation of MoO3 and Ag electrode using the Kurt J. Lesker Nano36 Thermal Evaporator System.

Device Characterization. The current density (J-V) curves were characterized by using an automated Solar Cell I–V Test System (Ossila) under AM 1.5G illumination (100 mW/cm) with a class AAA solar simulator from Newport under a glovebox-free or ambient

environment. Before each test, the solar simulator was calibrated by reference single-crystal Si cells (Sciencetech). For each condition, a total of 8 pixels or devices with an active area of 0.04 cm² were tested. A mismatch factor was not applied for calculating the device performance.

Solution Characterization Using CPOM. Solution characterization under CPOM was performed by sandwiching the polymer solutions between two microscope glass coverslips placed on a Si wafer during the CPOM measurements using the reflection mode. High-concentration solutions were obtained by the drop and dry method, where the concentration of the pristine solution is increased by drying a certain amount of solution and then adding 1 μ L of the solution to the dried droplet and mixing the solution by shearing with the microscope cover glasses to increase the concentration. For instance, a 200 mg/mL solution was achieved by drying 9 μ L of 20 mg/mL solution and adding 1 μ L of solution to increase the concentration of 20 mg/mL solution by 10-fold. The solution samples then underwent thermal annealing cycles to reach an equilibrium state before imaging under CPOM.

GIWAXS. GIWAXS measurements were performed at the 7.3.3 beamline of the Advanced Light Source at Lawrence Berkeley National Laboratory using incident angles of 0.08, 0.1, 0.12, and 0.14° with an Xray energy of 10 keV and a beam size of 30 μ m \times 50 μ m. All samples were placed in a helium chamber for measurement. For sample preparation, ZnO was first deposited on a Si wafer, followed by the photoactive layer deposition and thermal annealing in the same way that all OSC devices were fabricated. From GIWAXS measurement, 2D scattering images were obtained and converted to 1D linecut profiles by using the beamline NIKA package in Igor Pro. 84 The Ewald sphere correction (missing wedge correction) for the 2D images was obtained using the WAXSTools plugin⁸⁵ in Igor Pro. For molecular orientation analysis, pole figures are constructed by plotting the geometrically corrected intensity of the (010) peak from 5° sector cut profiles from the scattering patterns within the range of $10^{\circ} < \chi < 80^{\circ}$. The intensity of the (010) peak at each χ angle was determined by Gaussian peak deconvolution analysis. For rDoC analysis, the geometrically corrected intensities were integrated over χ and normalized by the total illumination volume (thickness and area of the sample) as previously

RSoXS. RSoXS data were collected at the National Synchrotron Light Source II at beamline 7-ID-1 in the transmission geometry. For sample preparation, the photoactive layer was blade-coated and thermally annealed using the same device fabrication conditions on a polystyrenesulfonate (PSS) film, which was spin-coated from a 10% PSS solution in water. The PSS solution was stirred overnight at room temperature before depositing on a Si wafer substrate. After photoactive layer deposition, the sample on a Si substrate was immersed in water, which dissolved the PSS layer and separated it from the substrate. The sample was then picked up with a 1 mm × 1 mm, 100 nm thick Si₃N₄ membrane supported on a 5 mm \times 5 mm, 200 μ m thick Si frame (Norcada) and transferred into the vacuum chamber for RSoXS measurement. RSoXS measurements were performed at beam energies from 270 to 290 eV with 5 s of exposure time per scan. The collected 2D scattering images were then converted into 1D profiles using the Nika package supported by the Igor Pro environment.

PiFM Measurements. The PiFM measurements were conducted using VistaScope from Molecular Vista, Inc. and using Pt-coated silicon cantilevers from Molecular Vista. Before starting the measurement, the laser power was recorded within the IR range of 733-1960 cm⁻¹, followed by the laser alignment using a parabolic mirror to ensure that the laser was focused on the tip of the cantilever. The wavelength of the quantum cascade laser (QCL) used for alignment was tuned to 1850 cm⁻¹ at an intensity of 20% of the recorded maximum power. For PiFM imaging, a scan size of 500 nm \times 500 nm with a pixel size of 256 \times 256 was used at a speed of 1 line/sec. During the measurement, the 1280 cm⁻¹ laser was tuned to <5% of the maximum power with 20–30 s duration per spectrum. To obtain PiFM spectra of the neat films, the QCL laser was first turned off to obtain only AFM topography images using a scan size of 1 μ m x 1 μ m. Afterward, the point spectra were obtained based on the collected AFM topography images with an IR intensity of <5% of the maximum power with 20-30 s duration per spectrum. The bulk FTIR spectra of neat materials using solid powder

samples were obtained using a Thermo Nicolet iS50 spectrometer as a comparison with the PiFM spectra on neat films.

c-AFM Measurements. Hole current mapping was conducted using an AIST-NT SmartSPM instrument on the XploRA-Nano system by Horiba, Inc. Budget sensors ContGB-G Au-coated conductive probes with a manufacturer-specified spring constant of 0.2 N m⁻¹ and a probe radius less than 25 nm were employed to record c-AFM scans. An applied probe-sample force ranged between 3 and 5 nN, with a substrate bias voltage of +3 V. High-work function top and bottom electrodes (PEDOT:PSS for hole transport layer and Au probe) were used to ensure hole-only transport.

Film Thickness Measurements. Film thickness was measured by using the Bruker Dektak XT profilometry with a 12.5 μ m radius stylus. During thickness measurements, a stylus force of 3 mg and a scan range of 1000–2000 μ m were used at a speed of 50 μ m/s. For thickness measurements, a part of the film was removed with a cotton swab with toluene. The thickness measurements were repeated in three to five different positions to obtain the average and standard deviation.

ASSOCIATED CONTENT

Supporting Information

The Supporting Information is available free of charge at https://pubs.acs.org/doi/10.1021/acs.chemmater.3c03055.

Solution characterization results including CPOM images; SAXS analysis details; WAXS measurement results; device measurement results at different coating temperatures; 2D GIWAXS patterns for the neat films and the corresponding linecut profiles; pole figures based on the molecular orientation analysis; and CPOM images of PM7 D2 solutions at different concentrations and films printed at evaporation and LL regimes (PDF)

In situ CPOM imaging of droplet drying process of PM7 D2 in CN (AVI)

In situ CPOM imaging during printing of PM7 D2 in TL +AN in the LL regime (AVI)

AUTHOR INFORMATION

Corresponding Author

Ying Diao — Department of Chemical and Biomolecular Engineering, University of Illinois at Urbana—Champaign, Urbana, Illinois 61801, United States; Beckman Institute, University of Illinois at Urbana—Champaign, Urbana, Illinois 61801, United States; orcid.org/0000-0002-8984-0051; Email: yingdiao@illinois.edu

Authors

Azzaya Khasbaatar — Department of Chemical and Biomolecular Engineering, University of Illinois at Urbana—Champaign, Urbana, Illinois 61801, United States; orcid.org/0000-0002-4145-3511

Austin L. Jones — School of Chemistry and Biochemistry, School of Materials Science and Engineering, Center for Organic Photonics and Electronics, Georgia Tech Polymer Network, Georgia Institute of Technology, Atlanta, Georgia 30332, United States

Pravini S. Fernando — Department of Chemical and Biomolecular Engineering, University of Illinois at Urbana—Champaign, Urbana, Illinois 61801, United States

Hiroaki Sai — Simpson Querrey Institute for BioNanotechnology, Northwestern University, Chicago, Illinois 60611, United States; Oorcid.org/0000-0002-4268-2148

Chenhui Zhu — Advanced Light Source, Lawrence Berkeley National Laboratory, Berkeley, California 94720, United States

Eliot Gann — Materials Measurement Laboratory, National Institute of Standards and Technology, Gaithersburg, Maryland 20899, United States

John R. Reynolds — School of Chemistry and Biochemistry, School of Materials Science and Engineering, Center for Organic Photonics and Electronics, Georgia Tech Polymer Network, Georgia Institute of Technology, Atlanta, Georgia 30332, United States; orcid.org/0000-0002-7417-4869

Complete contact information is available at: https://pubs.acs.org/10.1021/acs.chemmater.3c03055

Author Contributions

All authors have given approval to the final version of the manuscript.

Notes

The authors declare no competing financial interest.

ACKNOWLEDGMENTS

This work was primarily supported by the Office of Naval Research under grant numbers N00014-22-1-2202 (Y.D.) and N00014-22-1-2185 (J.R.R). A.K. acknowledges the A. T. Widiger Chemical Engineering fellowship. P.F. and Y.D. acknowledge support by the NSF CAREER award under Grant No. 18-47828. This research used resources of the Advanced Light Source, a U.S. DOE Office of Science User Facility under contract no. DE-AC02-05CH11231 and the LiX beamline at National Synchrotron Light Source II, which is part of the Center for BioMolecular Structure (CBMS) primarily supported by the National Institutes of Health, the National Institute of General Medical Sciences (NIGMS) through a P30 Grant (P30GM133893), and by the DOE Office of Biological and Environmental Research (KP1605010). LiX also received additional support from NIH Grant S10 OD012331. As part of NSLS-II, a national user facility at Brookhaven National Laboratory, work performed at the CBMS is supported in part by the U.S. Department of Energy, Office of Science, Office of Basic Energy Sciences Program under contract number DE-SC0012704. The research also used facilities of the Materials Research Laboratory Central Research Facilities, University of Illinois. The authors thank Dr. Lin Yang from the National Synchrotron Light Source II for support on SAXS measurements, Dr. Kathy Walsh from the Materials Research Laboratory at the University of Illinois for support on PiFM measurements, Dr. Aidan Coffey from Advanced Light Source for support on GIWAXS analysis, and Dr. Dean M. DeLongchamp from the National Institute of Standards and Technology for fruitful discussions on the interpretation of GIWAXS and RSoXS measurements.

REFERENCES

- (1) Fu, J.; Fong, P. W. K.; Liu, H.; Huang, C.-S.; Lu, X.; Lu, S.; Abdelsamie, M.; Kodalle, T.; Sutter-Fella, C. M.; Yang, Y.; Li, G. 19.31% Binary Organic Solar Cell and Low Non-Radiative Recombination Enabled by Non-Monotonic Intermediate State Transition. *Nat. Commun.* 2023, 14 (1), No. 1760.
- (2) Zhu, L.; Zhang, M.; Xu, J.; Li, C.; Yan, J.; Zhou, G.; Zhong, W.; Hao, T.; Song, J.; Xue, X.; Zhou, Z.; Zeng, R.; Zhu, H.; Chen, C.-C.; MacKenzie, R. C. I.; Zou, Y.; Nelson, J.; Zhang, Y.; Sun, Y.; Liu, F. Single-Junction Organic Solar Cells with over 19% Efficiency Enabled by a Refined Double-Fibril Network Morphology. *Nat. Mater.* **2022**, *21* (6), 656–663.
- (3) Wei, Y.; Chen, Z.; Lu, G.; Yu, N.; Li, C.; Gao, J.; Gu, X.; Hao, X.; Lu, G.; Tang, Z.; Zhang, J.; Wei, Z.; Zhang, X.; Huang, H. Binary

- Organic Solar Cells Breaking 19% via Manipulating the Vertical Component Distribution. *Adv. Mater.* **2022**, 34 (33), No. 2204718.
- (4) Cui, Y.; Xu, Y.; Yao, H.; Bi, P.; Hong, L.; Zhang, J.; Zu, Y.; Zhang, T.; Qin, J.; Ren, J.; Chen, Z.; He, C.; Hao, X.; Wei, Z.; Hou, J. Single-Junction Organic Photovoltaic Cell with 19% Efficiency. *Adv. Mater.* **2021**, 33 (41), No. 2102420.
- (5) Sun, R.; Wu, Y.; Yang, X.; Gao, Y.; Chen, Z.; Li, K.; Qiao, J.; Wang, T.; Guo, J.; Liu, C.; Hao, X.; Zhu, H.; Min, J. Single-Junction Organic Solar Cells with 19.17% Efficiency Enabled by Introducing One Asymmetric Guest Acceptor. *Adv. Mater.* 2022, 34 (26), No. 2110147. (6) Lee, S.; Jeong, D.; Kim, C.; Lee, C.; Kang, H.; Woo, H. Y.; Kim, B. J. Eco-Friendly Polymer Solar Cells: Advances in Green-Solvent
- J. Eco-Friendly Polymer Solar Cells: Advances in Green-Solvent Processing and Material Design. ACS Nano 2020, 14 (11), 14493–14527.
- (7) McDowell, C.; Bazan, G. C. Organic Solar Cells Processed from Green Solvents. *Curr. Opin. Green Sustainable Chem.* **2017**, *5*, 49–54.
- (8) Du, Z.; Luong, H. M.; Sabury, S.; Therdkatanyuphong, P.; Chae, S.; Welton, C.; Jones, A. L.; Zhang, J.; Peng, Z.; Zhu, Z.; Nanayakkara, S.; Coropceanu, V.; Choi, D. G.; Xiao, S.; Yi, A.; Kim, H. J.; Bredas, J.-L.; Ade, H.; Reddy, G. N. M.; Marder, S. R.; Reynolds, J. R.; Nguyen, T.-Q. Additive-Free Molecular Acceptor Organic Solar Cells Processed from a Biorenewable Solvent Approaching 15% Efficiency. *Mater. Horiz.* 2023, 10 (12), 5564–5576.
- (9) Mei, J.; Bao, Z. Side Chain Engineering in Solution-Processable Conjugated Polymers. *Chem. Mater.* **2014**, 26 (1), 604–615.
- (10) Khasbaatar, A.; Xu, Z.; Lee, J.-H.; Campillo-Alvarado, G.; Hwang, C.; Onusaitis, B. N.; Diao, Y. From Solution to Thin Film: Molecular Assembly of π -Conjugated Systems and Impact on (Opto)Electronic Properties. *Chem. Rev.* **2023**, *123* (13), 8395–8487.
- (11) Callaway, C. P.; Liu, A. L.; Venkatesh, R.; Zheng, Y.; Lee, M.; Meredith, J. C.; Grover, M.; Risko, C.; Reichmanis, E. The Solution Is the Solution: Data-Driven Elucidation of Solution-to-Device Feature Transfer for π -Conjugated Polymer Semiconductors. *ACS Appl. Mater. Interfaces* **2022**, *14* (3), 3613–3620.
- (12) Xu, Y.-C.; Ding, L.; Yao, Z.-F.; Shao, Y.; Wang, J.-Y.; Zhang, W.-B.; Pei, J. Conjugated Polymers in Solution: A Physical Perspective. *J. Phys. Chem. Lett.* **2023**, *14* (4), 927–939.
- (13) Yao, Z.-F.; Wang, J.-Y.; Pei, J. Controlling Morphology and Microstructure of Conjugated Polymers via Solution-State Aggregation. *Prog. Polym. Sci.* **2023**, *136*, No. 101626.
- (14) Kim, N.-K.; Jang, S.-Y.; Pace, G.; Caironi, M.; Park, W.-T.; Khim, D.; Kim, J.; Kim, D.-Y.; Noh, Y.-Y. High-Performance Organic Field-Effect Transistors with Directionally Aligned Conjugated Polymer Film Deposited from Pre-Aggregated Solution. *Chem. Mater.* **2015**, *27* (24), 8345–8353.
- (15) Zhao, K.; Zhang, Q.; Chen, L.; Zhang, T.; Han, Y. Nucleation and Growth of P(NDI2OD-T2) Nanowires via Side Chain Ordering and Backbone Planarization. *Macromolecules* **2021**, *54* (5), 2143–2154.
- (16) Park, Y. D.; Lee, H. S.; Choi, Y. J.; Kwak, D.; Cho, J. H.; Lee, S.; Cho, K. Solubility-Induced Ordered Polythiophene Precursors for High-Performance Organic Thin-Film Transistors. *Adv. Funct. Mater.* **2009**, *19* (8), 1200–1206.
- (17) Chen, M. S.; Lee, O. P.; Niskala, J. R.; Yiu, A. T.; Tassone, C. J.; Schmidt, K.; Beaujuge, P. M.; Onishi, S. S.; Toney, M. F.; Zettl, A.; Fréchet, J. M. J. Enhanced Solid-State Order and Field-Effect Hole Mobility through Control of Nanoscale Polymer Aggregation. *J. Am. Chem. Soc.* **2013**, *135* (51), 19229–19236.
- (18) Yao, Z.-F.; Wang, Z.-Y.; Wu, H.-T.; Lu, Y.; Li, Q.-Y.; Zou, L.; Wang, J.-Y.; Pei, J. Ordered Solid-State Microstructures of Conjugated Polymers Arising from Solution-State Aggregation. *Angew. Chem.* **2020**, 132 (40), 17620–17624.
- (19) Li, M.; An, C.; Marszalek, T.; Baumgarten, M.; Yan, H.; Müllen, K.; Pisula, W. Controlling the Surface Organization of Conjugated Donor–Acceptor Polymers by Their Aggregation in Solution. *Adv. Mater.* **2016**, 28 (42), 9430–9438.
- (20) Deng, J.; Zheng, L.; Ding, C.; Guo, Y.; Xie, Y.; Wang, J.; Ke, Y.; Li, M.; Li, L.; Janssen, R. A. J. Determinant Role of Solution-State Supramolecular Assembly in Molecular Orientation of Conjugated Polymer Films. *Adv. Funct. Mater.* **2023**, 33 (1), No. 2209195.

- (21) Bartelt, J. A.; Douglas, J. D.; Mateker, W. R.; Labban, A. E.; Tassone, C. J.; Toney, M. F.; Fréchet, J. M. J.; Beaujuge, P. M.; McGehee, M. D. Controlling Solution-Phase Polymer Aggregation with Molecular Weight and Solvent Additives to Optimize Polymer-Fullerene Bulk Heterojunction Solar Cells. *Adv. Energy Mater.* **2014**, *4* (9), No. 1301733.
- (22) van Franeker, J. J.; Turbiez, M.; Li, W.; Wienk, M. M.; Janssen, R. A. J. A Real-Time Study of the Benefits of Co-Solvents in Polymer Solar Cell Processing. *Nat. Commun.* **2015**, *6* (1), No. 6229.
- (23) Yi, X.; Peng, Z.; Xu, B.; Seyitliyev, D.; Ho, C. H. Y.; Danilov, E. O.; Kim, T.; Reynolds, J. R.; Amassian, A.; Gundogdu, K.; Ade, H.; So, F. Critical Role of Polymer Aggregation and Miscibility in Nonfullerene-Based Organic Photovoltaics. *Adv. Energy Mater.* **2020**, *10* (8), No. 1902430.
- (24) Wang, T.; Brédas, J.-L. Organic Photovoltaics: Understanding the Preaggregation of Polymer Donors in Solution and Its Morphological Impact. *J. Am. Chem. Soc.* **2021**, *143* (4), 1822–1835.
- (25) Khasbaatar, A.; Cheng, A.; Jones, A. L.; Kwok, J. J.; Park, S. K.; Komar, J. K.; Lin, O.; Jackson, N. E.; Chen, Q.; DeLongchamp, D. M.; Reynolds, J. R.; Diao, Y. Solution Aggregate Structures of Donor Polymers Determine the Morphology and Processing Resiliency of Non-Fullerene Organic Solar Cells. *Chem. Mater.* **2023**, 35 (7), 2713–2729.
- (26) Nahid, M. M.; Welford, A.; Gann, E.; Thomsen, L.; Sharma, K. P.; McNeill, C. R. Nature and Extent of Solution Aggregation Determines the Performance of P(NDI2OD-T2) Thin-Film Transistors. *Adv. Electron. Mater.* **2018**, *4* (4), No. 1700559.
- (27) Zheng, Y.-Q.; Yao, Z.-F.; Lei, T.; Dou, J.-H.; Yang, C.-Y.; Zou, L.; Meng, X.; Ma, W.; Wang, J.-Y.; Pei, J. Unraveling the Solution-State Supramolecular Structures of Donor—Acceptor Polymers and Their Influence on Solid-State Morphology and Charge-Transport Properties. *Adv. Mater.* **2017**, *29* (42), No. 1701072.
- (28) Park, K. S.; Luo, X.; Kwok, J. J.; Khasbaatar, A.; Mei, J.; Diao, Y. Subtle Molecular Changes Largely Modulate Chiral Helical Assemblies of Achiral Conjugated Polymers by Tuning Solution-State Aggregation. *ACS Cent. Sci.* **2023**, *9* (11), 2096–2107.
- (29) Xu, Z.; Park, K. S.; Kwok, J. J.; Lin, O.; Patel, B. B.; Kafle, P.; Davies, D. W.; Chen, Q.; Diao, Y. Not All Aggregates Are Made the Same: Distinct Structures of Solution Aggregates Drastically Modulate Assembly Pathways, Morphology, and Electronic Properties of Conjugated Polymers. *Adv. Mater.* 2022, 34 (32), No. 2203055.
- (30) Jones, A. L.; Yi Ho, C. H.; Riley, P. R.; Angunawela, I.; Ade, H.; So, F.; Reynolds, J. R. Investigating the Active Layer Thickness Dependence of Non-Fullerene Organic Solar Cells Based on PM7 Derivatives. *J. Mater. Chem. C* **2020**, 8 (43), 15459–15469.
- (31) Liu, Q.; Jiang, Y.; Jin, K.; Qin, J.; Xu, J.; Li, W.; Xiong, J.; Liu, J.; Xiao, Z.; Sun, K.; Yang, S.; Zhang, X.; Ding, L. 18% Efficiency Organic Solar Cells. *Sci. Bull.* **2020**, *65* (4), 272–275.
- (32) Larsen, C.; Lundberg, P.; Tang, S.; Ràfols-Ribé, J.; Sandström, A.; Mattias Lindh, E.; Wang, J.; Edman, L. A Tool for Identifying Green Solvents for Printed Electronics. *Nat. Commun.* **2021**, *12* (1), No. 4510.
- (33) Alder, C. M.; Hayler, J. D.; Henderson, R. K.; Redman, A. M.; Shukla, L.; Shuster, L. E.; Sneddon, H. F. Updating and Further Expanding GSK's Solvent Sustainability Guide. *Green Chem.* **2016**, *18* (13), 3879–3890.
- (34) Henderson, R. K.; Jiménez-González, C.; Constable, D. J. C.; Alston, S. R.; Inglis, G. G. A.; Fisher, G.; Sherwood, J.; Binks, S. P.; Curzons, A. D. Expanding GSK's Solvent Selection Guide Embedding Sustainability into Solvent Selection Starting at Medicinal Chemistry. *Green Chem.* **2011**, *13* (4), 854–862.
- (35) Jiménez-González, C.; Curzons, A. D.; Constable, D. J. C.; Cunningham, V. L. Expanding GSK's Solvent Selection Guide—Application of Life Cycle Assessment to Enhance Solvent Selections. *Clean Technol. Environ. Policy* **2004**, *7* (1), 42–50.
- (36) National Center for Biotechnology Information. PubChem. Compound Summary for CID 7519, Anisole. https://pubchem.ncbi.nlm.nih.gov/compound/7519 (accessed 05 Oct, 2023).

- (37) Hansen, C. M. The Three Dimensional Solubility Parameter and Solvent Diffusion Coefficient: Their Importance in Surface Coating Formulation; Danish Technical Press, 1967.
- (38) Jackson, N. E.; Kohlstedt, K. L.; Savoie, B. M.; Olvera de la Cruz, M.; Schatz, G. C.; Chen, L. X.; Ratner, M. A. Conformational Order in Aggregates of Conjugated Polymers. *J. Am. Chem. Soc.* **2015**, *137* (19), 6254–6262.
- (39) Krevelen, D. W. van.; Dirk, W.; Hoftyzer, P. J. Properties of Polymers, Their Estimation and Correlation with Chemical Structure, 2nd completely rev. ed.; Elsevier Scientific Pub. Co.: Amsterdam, 1976.
- (40) Traiphol, R.; Sanguansat, P.; Srikhirin, T.; Kerdcharoen, T.; Osotchan, T. Spectroscopic Study of Photophysical Change in Collapsed Coils of Conjugated Polymers: Effects of Solvent and Temperature. *Macromolecules* **2006**, *39* (3), 1165–1172.
- (41) Newbloom, G. M.; Hoffmann, S. M.; West, A. F.; Gile, M. C.; Sista, P.; Cheung, H.-K. C.; Luscombe, C. K.; Pfaendtner, J.; Pozzo, L. D. Solvatochromism and Conformational Changes in Fully Dissolved Poly(3-Alkylthiophene)s. *Langmuir* **2015**, *31* (1), 458–468.
- (42) Steyrleuthner, R.; Schubert, M.; Howard, I.; Klaumünzer, B.; Schilling, K.; Chen, Z.; Saalfrank, P.; Laquai, F.; Facchetti, A.; Neher, D. Aggregation in a High-Mobility n-Type Low-Bandgap Copolymer with Implications on Semicrystalline Morphology. *J. Am. Chem. Soc.* **2012**, 134 (44), 18303–18317.
- (43) Scharsich, C.; Lohwasser, R. H.; Sommer, M.; Asawapirom, U.; Scherf, U.; Thelakkat, M.; Neher, D.; Köhler, A. Control of Aggregate Formation in Poly(3-Hexylthiophene) by Solvent, Molecular Weight, and Synthetic Method. *J. Polym. Sci., B: Polym. Phys.* **2012**, 50 (6), 442–452
- (44) Balooch Qarai, M.; Chang, X.; Spano, F. C. Vibronic Exciton Model for Low Bandgap Donor—Acceptor Polymers. *J. Chem. Phys.* **2020**, *153* (24), No. 244901.
- (45) Arunagiri, L.; Zhang, G.; Hu, H.; Yao, H.; Zhang, K.; Li, Y.; Chow, P. C. Y.; Ade, H.; Yan, H. Temperature-Dependent Aggregation Donor Polymers Enable Highly Efficient Sequentially Processed Organic Photovoltaics Without the Need of Orthogonal Solvents. *Adv. Funct. Mater.* **2019**, 29 (33), No. 1902478.
- (46) Liu, C.; Hu, W.; Jiang, H.; Liu, G.; Han, C. C.; Sirringhaus, H.; Boué, F.; Wang, D. Chain Conformation and Aggregation Structure Formation of a High Charge Mobility DPP-Based Donor—Acceptor Conjugated Polymer. *Macromolecules* **2020**, *53* (19), 8255—8266.
- (47) Kwok, J. J.; Park, K. S.; Patel, B. B.; Dilmurat, R.; Beljonne, D.; Zuo, X.; Lee, B.; Diao, Y. Understanding Solution State Conformation and Aggregate Structure of Conjugated Polymers via Small Angle X-Ray Scattering. *Macromolecules* **2022**, *55* (11), 4353–4366.
- (48) Xi, Y.; M Wolf, C.; D Pozzo, L. Self-Assembly of Donor–Acceptor Conjugated Polymers Induced by Miscible 'Poor' Solvents. *Soft Matter* **2019**, *15* (8), 1799–1812.
- (49) Chen, C.-Y.; Chan, S.-H.; Li, J.-Y.; Wu, K.-H.; Chen, H.-L.; Chen, J.-H.; Huang, W.-Y.; Chen, S.-A. Formation and Thermally-Induced Disruption of Nanowhiskers in Poly(3-Hexylthiophene)/Xylene Gel Studied by Small-Angle X-Ray Scattering. *Macromolecules* **2010**, 43 (17), 7305–7311.
- (50) Li, Y.-C.; Chen, K.-B.; Chen, H.-L.; Hsu, C.-S.; Tsao, C.-S.; Chen, J.-H.; Chen, S.-A. Fractal Aggregates of Conjugated Polymer in Solution State. *Langmuir* **2006**, 22 (26), 11009–11015.
- (51) Ovchinnikov, Y. K.; Antipov, E. M.; Markova, G. S.; Bakeev, N. F. Comparative Investigation of Short-Range Order in Unbranched Alkanes and Polyethylene. *Makromol. Chem.* **1976**, 177 (5), 1567–1581.
- (52) Lee, S. H.; Saito, N.; Takai, O. The Importance of Precursor Molecules Symmetry in the Formation of Self-Assembled Monolayers. *Jpn. J. Appl. Phys.* **2007**, *46* (3R), 1118.
- (53) Zhou, Y.-Y.; Xu, Y.-C.; Yao, Z.-F.; Li, J.-Y.; Pan, C.-K.; Lu, Y.; Yang, C.-Y.; Ding, L.; Xiao, B.-F.; Wang, X.-Y.; Shao, Y.; Zhang, W.-B.; Wang, J.-Y.; Wang, H.; Pei, J. Visualizing the Multi-Level Assembly Structures of Conjugated Molecular Systems with Chain-Length Dependent Behavior. *Nat. Commun.* 2023, 14 (1), No. 3340.
- (54) Yao, Z.-F.; Zheng, Y.-Q.; Li, Q.-Y.; Lei, T.; Zhang, S.; Zou, L.; Liu, H.-Y.; Dou, J.-H.; Lu, Y.; Wang, J.-Y.; Gu, X.; Pei, J. Wafer-Scale

- Fabrication of High-Performance n-Type Polymer Monolayer Transistors Using a Multi-Level Self-Assembly Strategy. *Adv. Mater.* **2019**, 31 (7), No. 1806747.
- (55) Liu, Y.; Zhao, J.; Li, Z.; Mu, C.; Ma, W.; Hu, H.; Jiang, K.; Lin, H.; Ade, H.; Yan, H. Aggregation and Morphology Control Enables Multiple Cases of High-Efficiency Polymer Solar Cells. *Nat. Commun.* **2014**, *5* (1), No. 5293.
- (56) Hu, H.; Chow, P. C. Y.; Zhang, G.; Ma, T.; Liu, J.; Yang, G.; Yan, H. Design of Donor Polymers with Strong Temperature-Dependent Aggregation Property for Efficient Organic Photovoltaics. *Acc. Chem. Res.* 2017, 50 (10), 2519–2528.
- (57) Kim, Y.-J.; Lee, S.; Niazi, M. R.; Hwang, K.; Tang, M.-C.; Lim, D.-H.; Kang, J.-S.; Smilgies, D.-M.; Amassian, A.; Kim, D.-Y. Systematic Study on the Morphological Development of Blade-Coated Conjugated Polymer Thin Films via In Situ Measurements. *ACS Appl. Mater. Interfaces* **2020**, *12* (32), 36417–36427.
- (58) Thompson, B. C.; Fréchet, J. M. J. Polymer–Fullerene Composite Solar Cells. *Angew. Chem., Int. Ed.* **2008**, 47 (1), 58–77.
- (59) Diao, Y.; Zhou, Y.; Kurosawa, T.; Shaw, L.; Wang, C.; Park, S.; Guo, Y.; Reinspach, J. A.; Gu, K.; Gu, X.; Tee, B. C. K.; Pang, C.; Yan, H.; Zhao, D.; Toney, M. F.; Mannsfeld, S. C. B.; Bao, Z. Flow-Enhanced Solution Printing of All-Polymer Solar Cells. *Nat. Commun.* **2015**, *6* (1), No. 7955.
- (60) Huang, Y.; Kramer, E. J.; Heeger, A. J.; Bazan, G. C. Bulk Heterojunction Solar Cells: Morphology and Performance Relationships. *Chem. Rev.* **2014**, *114* (14), 7006–7043.
- (61) Qu, G.; Park, K. S.; Kafle, P.; Zhang, F.; Kwok, J. J.; Patel, B. B.; Smilgies, D.-M.; Thomsen, L.; McNeill, C. R.; Diao, Y. Lyotropic Liquid Crystalline Mesophase Governs Interfacial Molecular Orientation of Conjugated Polymer Thin Films. *Chem. Mater.* **2020**, 32 (14), 6043–6054.
- (62) Zhang, F.; Mohammadi, E.; Qu, G.; Dai, X.; Diao, Y. Orientation-Dependent Host–Dopant Interactions for Manipulating Charge Transport in Conjugated Polymers. *Adv. Mater.* **2020**, 32 (39), No. 2002823.
- (63) White, J. L.; Spruiell, J. E. The Specification of Orientation and Its Development in Polymer Processing. *Polym. Eng. Sci.* **1983**, 23 (5), 247–256.
- (64) Hermans, P. H.; Hermans, J. J.; Vermans, D.; Weidinger, A. Deformation Mechanism of Cellulose Gels. IV. General Relationship between Orientation of the Crystalline and That of the Amorphous Portion. J. Polym. Sci. 1948, 3 (1), 1–9.
- (65) Rivnay, J.; Noriega, R.; Kline, R. J.; Salleo, A.; Toney, M. F. Quantitative Analysis of Lattice Disorder and Crystallite Size in Organic Semiconductor Thin Films. *Phys. Rev. B* **2011**, *84* (4), No. 045203.
- (66) Rivnay, J.; Mannsfeld, S. C. B.; Miller, C. E.; Salleo, A.; Toney, M. F. Quantitative Determination of Organic Semiconductor Microstructure from the Molecular to Device Scale. *Chem. Rev.* **2012**, *112* (10), 5488–5519.
- (67) Bridges, C. R.; Ford, M. J.; Popere, B. C.; Bazan, G. C.; Segalman, R. A. Formation and Structure of Lyotropic Liquid Crystalline Mesophases in Donor–Acceptor Semiconducting Polymers. *Macromolecules* **2016**, 49 (19), 7220–7229.
- (68) Park, K. S.; Kwok, J. J.; Dilmurat, R.; Qu, G.; Kafle, P.; Luo, X.; Jung, S.-H.; Olivier, Y.; Lee, J.-K.; Mei, J.; Beljonne, D.; Diao, Y. Tuning Conformation, Assembly, and Charge Transport Properties of Conjugated Polymers by Printing Flow. *Sci. Adv.* **2019**, *5* (8), No. eaaw7757.
- (69) Le Berre, M.; Chen, Y.; Baigl, D. From Convective Assembly to Landau—Levich Deposition of Multilayered Phospholipid Films of Controlled Thickness. *Langmuir* **2009**, *25* (5), 2554—2557.
- (70) Qu, G.; Kwok, J. J.; Mohammadi, E.; Zhang, F.; Diao, Y. Understanding Film-To-Stripe Transition of Conjugated Polymers Driven by Meniscus Instability. *ACS Appl. Mater. Interfaces* **2018**, *10* (47), 40692–40701.
- (71) van Franeker, J. J.; Heintges, G. H. L.; Schaefer, C.; Portale, G.; Li, W.; Wienk, M. M.; van der Schoot, P.; Janssen, R. A. J. Polymer Solar

- Cells: Solubility Controls Fiber Network Formation. *J. Am. Chem. Soc.* **2015**, *137* (36), *11783*–11794.
- (72) Collins, B. A.; Cochran, J. E.; Yan, H.; Gann, E.; Hub, C.; Fink, R.; Wang, C.; Schuettfort, T.; McNeill, C. R.; Chabinyc, M. L.; Ade, H. Polarized X-Ray Scattering Reveals Non-Crystalline Orientational Ordering in Organic Films. *Nat. Mater.* **2012**, *11* (6), 536–543.
- (73) Collins, B. A.; Gann, E. Resonant Soft X-Ray Scattering in Polymer Science. *J. Polym. Sci.* **2022**, *60* (7), 1199–1243.
- (74) Debye, P.; Anderson, H. R.; Brumberger, H. Scattering by an Inhomogeneous Solid. II. The Correlation Function and Its Application. *J. Appl. Phys.* **1957**, 28 (6), 679–683.
- (75) Chen, Z.; Chen, X.; Qiu, B.; Zhou, G.; Jia, Z.; Tao, W.; Li, Y.; Yang, Y. M.; Zhu, H. Ultrafast Hole Transfer and Carrier Transport Controlled by Nanoscale-Phase Morphology in Nonfullerene Organic Solar Cells. J. Phys. Chem. Lett. 2020, 11 (9), 3226–3233.
- (76) Gu, K. L.; Zhou, Y.; Morrison, W. A.; Park, K.; Park, S.; Bao, Z. Nanoscale Domain Imaging of All-Polymer Organic Solar Cells by Photo-Induced Force Microscopy. *ACS Nano* **2018**, *12* (2), 1473–1481.
- (77) Qiu, B.; Xue, L.; Yang, Y.; Bin, H.; Zhang, Y.; Zhang, C.; Xiao, M.; Park, K.; Morrison, W.; Zhang, Z.-G.; Li, Y. All-Small-Molecule Nonfullerene Organic Solar Cells with High Fill Factor and High Efficiency over 10%. *Chem. Mater.* **2017**, 29 (17), 7543–7553.
- (78) Fernando, P. S.; Mehta, J. S.; Smilgies, D.-M.; Mativetsky, J. M. Probing the Contribution of Lateral Pathways to Out-of-Plane Charge Transport in Organic Bulk Heterojunctions. *Adv. Electron. Mater.* **2022**, 8 (9), No. 2200156.
- (79) Mehta, J. S.; Mativetsky, J. M. In-Plane Pathways Facilitate Out-of-Plane Charge Transport in Organic Solar Cell Active Layers. *ACS Appl. Energy Mater.* **2018**, *1* (10), 5656–5662.
- (80) Zhao, H.; Naveed, H. B.; Lin, B.; Zhou, X.; Yuan, J.; Zhou, K.; Wu, H.; Guo, R.; Scheel, M. A.; Chumakov, A.; Roth, S. V.; Tang, Z.; Müller-Buschbaum, P.; Ma, W. Hot Hydrocarbon-Solvent Slot-Die Coating Enables High-Efficiency Organic Solar Cells with Temperature-Dependent Aggregation Behavior. *Adv. Mater.* **2020**, 32 (39), No. 2002302.
- (81) Yang, L.; Liu, J.; Chodankar, S.; Antonelli, S.; DiFabio, J. Scanning Structural Mapping at the Life Science X-Ray Scattering Beamline. *J. Synchrotron Radiat.* **2022**, 29 (2), 540–548.
- (82) Yang, L.; Antonelli, S.; Chodankar, S.; Byrnes, J.; Lazo, E.; Qian, K. Solution Scattering at the Life Science X-Ray Scattering (LiX) Beamline. J. Synchrotron Radiat. 2020, 27 (3), 804–812.
- (83) Park, K. S.; Xue, Z.; Patel, B. B.; An, H.; Kwok, J. J.; Kafle, P.; Chen, Q.; Shukla, D.; Diao, Y. Chiral Emergence in Multistep Hierarchical Assembly of Achiral Conjugated Polymers. *Nat. Commun.* **2022**, *13* (1), No. 2738.
- (84) Ilavsky, J. N. Software for Two-Dimensional Data Reduction. J. Appl. Crystallogr. 2012, 45 (2), 324–328.
- (85) Oosterhout, S. D.; Savikhin, V.; Zhang, J.; Zhang, Y.; Burgers, M. A.; Marder, S. R.; Bazan, G. C.; Toney, M. F. Mixing Behavior in Small Molecule:Fullerene Organic Photovoltaics. *Chem. Mater.* **2017**, 29 (7), 3062–3069.